In-situ picosecond time-resolved probing of magnetization dynamics in polycrystalline ferromagnetic thin films

BY

Jonathan Rudge

Bachelor of Science, University of Victoria 2001
Bachelor of Education, University of Victoria 2003

Submitted to the University of Victoria
in partial fulfillment of
the requirements for the degree of

Master of Science

in

Physics

In-situ picosecond time-resolved probing of magnetization dynamics in polycrystalline ferromagnetic thin films

BY

Jonathan Rudge

Bachelor of Science, University of Victoria 2001

Bachelor of Education, University of Victoria 2003

Superivisory Committee

Dr. Byoung C. Choi, Supervisor
(Dept. of Physics)

Dr. Geoffrey M. Steeves, Departmental Member
(Dept. of Physics)

Dr. Alexandre Brolo, Outside Member
(Dept. of Chemistry)

Superivisory Committee

Dr. Byoung C. Choi, Supervisor
(Dept. of Physics)

Dr. Geoffrey M. Steeves, Departmental Member
(Dept. of Physics)

Dr. Alexandre Brolo, Outside Member
(Dept. of Chemistry)

ABSTRACT

Magnetization dynamics in polycrystalline Permalloy thin films were studied in-situ using a time-resolved magneto-optic Kerr effect microscope (TR-MOKE). The films, in thicknesses from 9 to 22 nm, were thermally evaporated in a high-vacuum ($<10^{-8}$ mbar) environment. Two important dynamic parameters of the magnetization, the precessional frequency and effective damping constant α_{eff}, are obtained from the picosecond time-resolved evolution of the magnetization after a magnetic field pulse excitation. For all film thicknesses investigated, the magnetization carried out precessional motion at a frequency of ~2 GHz. The effective damping constant α_{eff} is extracted from the precessional decay time τ. The decay time is obtained by fitting the experimental time trace of the magnetization to a damped sine function of the form $M(t)=Mo\ e^{-t/\tau}\ \sin(\omega t - \phi)$, where ω is the angular frequency of the precession mode and ϕ is the initial phase of the precession. For the thinnest film investigated, α_{eff} reaches the value of 0.32, considerably higher than any previously reported values. The physical origin of the increased magnetic damping is discussed in terms of the surface roughness induced extrinsic damping in magnetic thin films, but the experimentally found thickness-dependence of α_{eff}, however, does not agree with the prediction. The discrepancy is attributed to the percolation of Permalloy islands into connected clusters occurring at the thickness of ~18 nm.

Table of Contents

List of Tables

List of Figures

Acknowledgments

A large number of people have helped me along the way and without their help this would never have been possible. To highlight just a few of the many Dave Smith for showing me how to make the parts I needed without losing any fingers, to Paul Birney for lending me various components and then showing me how to use them, Joe Kolthammer and Albert Santoni for commiseration and comments, and all of the wonderful administrative people both past and present. Finally special thanks to Dr. Byoung Choi for his experience, guidance, and patience (not necessarily in that order.)

Chapter 1

Motivation

The study of magnetism and magnetic phenomenon is of tremendous technical importance. This was officially recognized by the noble prize committee when they awarded the 2007 Nobel Prize in Physics to Albert Fert and Peter Grünberg, "for the discovery of Giant Magnetoresistance (GMR)."[1] . The full truth is probably better realized by looking at Moore's law [2], which states that the rate of technological increase is roughly exponential, doubling approximately every two years.[1] Although this phenomenal rate of growth may seem impossible to sustain it has been maintained for over forty years now and seems poised to continue into the next decade. This astounding rate of growth is the result of an ever increasing demand in every sector where technology is or can be applied. To produce higher density storage media, which can keep pace with this growth, requires a more sophisticated understanding and better control of the magnetic properties of materials. In addition the lure of spin based electronic devices (spintronics as it has come to be known) and better memories (MRAM's, magnetic random access memories) help to drive research in this field.

Underlying the commercial and technical importance of understanding magnetism is the pure science of magnetism. Although it might be easy to forget about this aspect of the research, magnetism is clearly deserving of study as purely scientific pursuit. It is one of only a handful of macroscopically observable quantum mechanical phenomena.

[1] Technically Dr. Moore was only writing about the number of transistors that could be economically placed on a single chip. Other people's names are associated with other versions of this idea but they all follow the trend noted by Moore. This is not unreasonable given the interdependency of the differing technologies particularly in the computer industry.

Superfluidity, superconductivity, Bose-Einstein condensates, and nuclear reactions are the only other examples of macroscopic quantum effects. Of these candidates it is only one of two seen under ordinary circumstances and the only one readily observable without special equipment.

Chapter 2

Background

2.1 Domains and Magnetism

Most people would agree that modern magnetism began with Weiss[3]. He proposed that a ferromagnetic material could be comprised of a large number of small regions called domains. Within each domain the magnetization is aligned as a result of a molecular field or Weiss field, (now known as the exchange field,) but the alignment of the different domains within a sample can vary relative to each other. A sample is unmagnetized when the domains are randomly aligned to each other so that the vector addition of all the domains is zero. When an external field is applied to an unmagnetized sample the domains begin to align with the external field. As the magnetization increases more and more of the domains align with the field and the magnetization of the sample increases. When all the domains are aligned the magnetization of the sample plateaus, this is called the saturation magnetization (Ms). When the applied field is removed most of the domains remain aligned, (with some few moving to reduce the overall energy,) and so there is a net magnetization in the absence of any applied field which is called the remanence.

Weiss's idea of the molecular field was based on observations and not any particular theory. We now know that the origin of the field he proposed is in fact quantum mechanical in nature and has no classical analogue. Robert M. White gives a very good treatment of the quantum mechanics which lead to this [4], however a simplified explanation of this is the following:. Consider a system of two interacting electrons, we can write the wavefunction of the system as a product of space and spin functions.

$$\Psi_{tot} = \Psi(r_1, r_2)\varphi(s_1, s_2) \tag{2.1}$$

Since the total wavefunction of the two electron system must be antisymmetric (electrons are fermions after all) this implies that if the spin component ϕ is antisymmetric the space component (Ψ) is symmetric and vice versa. If the space function is symmetric it must have the form (neglecting the normalization constant):

$$\Psi_{sym} = \Psi_a(r_1)\Psi_b(r_2) + \Psi_b(r_1)\Psi_a(r_2) \tag{2.2}$$

Similarly the antisymmetric space function will have the form,

$$\Psi_{asym} = \Psi_a(r_1)\Psi_b(r_2) - \Psi_b(r_1)\Psi_a(r_2) \tag{2.3}$$

Each of the above wavefunctions will yield an energy eigenvalue (E_{sym}, E_{asym}) with the difference between the two energies corresponding to the difference in energy between parallel and antiparallel alignments of the spins.

$$E_{sym} - E_{asym} = 2J \tag{2.4}$$

Finally we note that the energy equation for two interacting electrons can be expanded to yield an exchange energy term, (in addition to two terms not shown for the separate electrons and a cross term which is the coulombic energy term,) so named because it results from exchanging the two electrons. (Neglecting the normalization constant and assuming that the combined wavefunction is a linear combination of the individual wavefunctions.) :

$$E_{ex} = \int\int \Psi_a^*(r_1)\Psi_b^*(r_2)\langle\mathcal{H}_{12}\rangle\Psi_b(r_1)\Psi_a(r_2)d\tau_1 d\tau_2 \tag{2.5}$$

Since this is the only part of the energy equation that relies on particle exchange we can directly relate it to the J in equation 2.4. If J is positive then the symmetric wavefunction is a higher energy state and the antisymmetric space state is preferred. This implies the spin

state will be symmetric, i.e. the spins align parallel - a ferromagnetic ordering. Alternatively if J is negative antiferromagnetic ordering arises. At this point the Hamiltonian one usually encounters is the Heisenberg Hamiltonian:

$$\mathcal{H}_{Heis} = -\sum_{i,j} J_{i,j} \mathbf{S}_i \circ \mathbf{S}_j \tag{2.6}$$

where the $\mathbf{S}$'s refer to the spins and $J_{i,j}$ is the exchange interaction integral. Unfortunately, as with many quantum mechanical problems, an exact solution is not available. On the other hand approximations can be made that allow the quantum mechanical formulation to be recast into a pseudo-classical form and it is these approximations that form the basis for most of the micromagnetic simulation work that has been done to date. Having touched on the origins of the exchange interaction we turn our attention to more physical aspects.

2.2 Techniques to observe magnetic domains

Over the years since Weiss proposed the idea of domains and the molecular field, (and quantum mechanics explained the origins of it,) a variety of techniques have been developed to study magnetic phenomena. A brief description of some of these techniques is given here. This is by no means an exhaustive list as the intent is to give an overview. More details of each technique are given in the associated references, with the last reference in each part being a review of the relevant technique.

The Bittter technique was the first experimental technique available [5-7]. It consists of spreading a fine magnetic powder on the surface of a magnet. The powder then aligns itself to the stray fields on the surface revealing the domain structure of the magnetic surface. It is a mature technique now and papers usually report using it in conjunction with other techniques since there is clearly no temporal resolution. The spatial resolution is limited by the grain size of the applied powder. Traditionally this has limited the spatial resolution to the micron range however the availability of nanoscale colloids has pushed this lower limt to

a 100 nm using electron microscopy. This has caused a small resurgence in this technique since it is very simple to perform and requires no specialized equipment.

Scanning electron microscope with polarization analysis, (SEMPA) is another technique for analyzing magnetic domains having a lower resolution of about 50 nm [8-10]. This technique is difficult to implement and has largely been usurped by MFM, so is not very common. It relies on the spin polarization of electrons reflected from a magnetized surface. Since the percentage of polarization is quite low good contrast is difficult to achieve. It does however allow one to study the magnetization directly rather than looking at the stray fields but it also has no temporal resolution.

Magnetic Force Microscopy (MFM), although much more recent, might be classified as a variant of the Bitter technique [11-13]. MFM which is a variant of atomic force microscopy (AFM) does not use a powder to measure the stray field but instead uses an AFM tip coated in a magnetic material to achieve the same result. Although MFM has a higher spatial resolution (~100 nm) than the traditional Bitter technique (on a par with its nanocolloid incarnation) and is close to that of SEMPA it has largely usurped the roles of both. It is a relative inexpensive and simple technique to implement and that has made it an indispensible tool for static investigations. Although it still has no temporal resolution to date the technique does not inherently preclude the possibility of a temporal mode. This might be accomplished by using a modified tapping mode with the magnetic excitations at some harmonic of the tapping frequency.

Spin polarized scanning tunneling electron microscopy (SP-STM), like MFM is a relative newcomer to the field of magnetics [14-16]. This technique relies on a thin layer of magnetic material over a normal STM tip, which then acts as a spin filter. Like the SEMPA it is difficult to implement because of the small fraction of polarization. It does have the advantage of very high spatial resolution (<1 nm) but has not yet been demonstrated with time resolved capability. This is currently being worked on by Dr. Freeman's group at the University of Alberta.

X-ray magneto-circular dichorism (XMCD) is another technique with high spatial reso-

lution, on the order of 50-100 nm [17-19]. It relies on the small energy splitting between spins to provide preferential absorption of X-Rays. By tuning and polarizing the x-ray source it is possible to obtain a beam which is absorbed by a particular element in a particular magnetization state. This makes XMCD element specific as well as magnetization sensitive. In addition it has been demonstrated with high temporal resolution (100 ps) as well making it a very powerful tool in the study of magnetic structures. The major drawback of this technique is the requirement for a high luminosity, tunable x-ray source. Currently this is only possible from syncnotron radiation sources which are certainly not readily available in every lab.

Brillouin light scattering (BLS) is another technique especially well suited for studying spin waves [20-22]. It is essentially a form of Raman spectroscopy with a higher resolution of the spectra. It analyzes the frequency shift in a light beam after interaction with a material, although the technique was originally developed for the study of phonons it has been used to study magnons and spin waves quite successfully. Unfortunately it has relatively limited spatial resolution temporal resolutions due to the low signal to noise ratio. Presently a 30 μm spatial resloution and a temporal resolution on the order of 1 ns.

Magneto-optic microscopes are probably the most common setups for investigating magnetization [23-25]. They can be setup to do either transmission (Faraday Effect) or reflection (Kerr effect), as well as having spatial scanning and temporal scanning functions. This instruments have been demonstrated with spatial resolutions <1 μm and temporal resolutions of 50 ps or less. Currently the spatial resolution is limited by the diffraction limit of the laser but the possibility of using a near field optical microscope presents the possibiltiy of pushing the spatial resolution to a 100 nm or less. Since the apparatus used in this investigation was a time-resolved magneto-optic Kerr effect microscope, more details on this class of instruments will be given. Magneto-optic microscopes rely upon the fact that the polarization of light is directly affected by a magnetic material.. Another way of saying this is that the reflection (and transmission) coefficients for left and right circularly polarized light are different depending on the magnetization of a material. Since the difference in

coefficients for any given material are directly proportional to the amount of magnetization present measuring the change in polarization of the reflected (or transmitted) light is a direct measure of the change in magnetization of a sample. A brief mathematical treatment is given in Appendix 1 for the interested reader but for here it is enough to know that the polarization state of a reflected (or transmitted) beam changes in proportion to the amount of magnetization present in the material being sampled. By using an intense light source (a laser) with a predetermined polarization state it is possible to determine the change in magnetization of a sample. There are of course limitations to this technique. First is that it is only sensitive to (in the case of reflection) the penetration depth of the light which is roughly 20 nm for our setup. Second is that the magnetization is not the only thing that can affect the polarization state. In order to be a useful tool changes in polarization caused by other effects need to be eliminated. Fortunately this is a relatively simple matter since a change in the magnetization is easy to produce by application of an external field which does not affect any of the other optical properties of a material. So by applying a slowly varying magnetic field to a sample and analyzing the change in polarization one can obtain information about the sample magnetization but not about the absolute state of the magnetization. How slow is slowly? In this case slowly is determined by how fast one can sample the polarization state of the reflected light. Ideally the sampling should be fast enough that the magnetization state does not change for the duration of each sample In the case of a quasi-static magneto-optic microscope, used for producing hysteresis loops, the field might sweep at 1Hz or less. If the sampling rate is 10 ms then one would get 100 points for each sweep of the field. On the other hand if the field sweeps at 1 ms and the sampling rate is 10 ms then there is going to be a problem since the magnetization state will have changed drastically during the sampling period. In the truly dynamic regime for which the current research is focused on the characteristic times are on the order of picoseconds so a slight variation is required. In essence it works exactly the same as the "static" version only the sampling rate has been dramatically reduced. By using an ultra short laser pulse,(~100fs,) the sampling rate is reduced which means that the sweep rate can be increased.

In the case of these experiments the sampling is accomplished by the probe beam with a temporal width of ~100 fs. The sweep is replaced by an excitation pulse referred to as the pump which has a typical temporal width on the order of nanoseconds. The technique is commonly referred to as a pump-probe technique and is schematically shown in figure 2-1. Some excellent reviews of this technique are readily available [26-27]. Application of the pump pulse moves the system out of equilibrium. By controlling the delay between the pump pulse and the probe pulse, the probe beam can measure the (nearly) instantaneous state of the process at successive points as it evolves in time. Although the cartoon makes it appear that the probe pulse is being changed relative to the pump pulse, in our set up the change in delay time is actually accomplished by changing the beginning of the pump pulse relative to a fixed probe time.

Given the preceding it is probably not surprising that the study of magnetism can be roughly divided into two main areas based on the sampling speed. Low sampling rates provide static or quasi-static information. Static and quasi-static studies are mostly concerned with magnetic energy densities of permanent magnets and the hysteresis loops of bulk materials. If there is a dynamic component in this area it is commonly associated with domain wall motion. This area should not be dismissed as trivial even today since improving these properties can lead to technical advances in power generation and conversion, but the focus of this research is dynamic so nothing more is going to be said about the static and quasi-static areas. If the sampling rate is high then it is possible to obtain information on the dynamic aspects of magnetization. Very early on the studies of domains and domain wall motion quickly showed that domain walls have a maximum velocity of travel (see Schryer and Walker [28]). This led to the obvious question of what happens when a magnetic material is subjected to a high frequency field.

It should be noted here that the question was far more than academic curiosity. Industry is at the very heart of the research. In the late fifties the industrial interest was largely centered on the idea of magnetic memory arrays. At that time these were arrays of ferrite cores. A field pulse generated by a current carrying wire was used to switch the

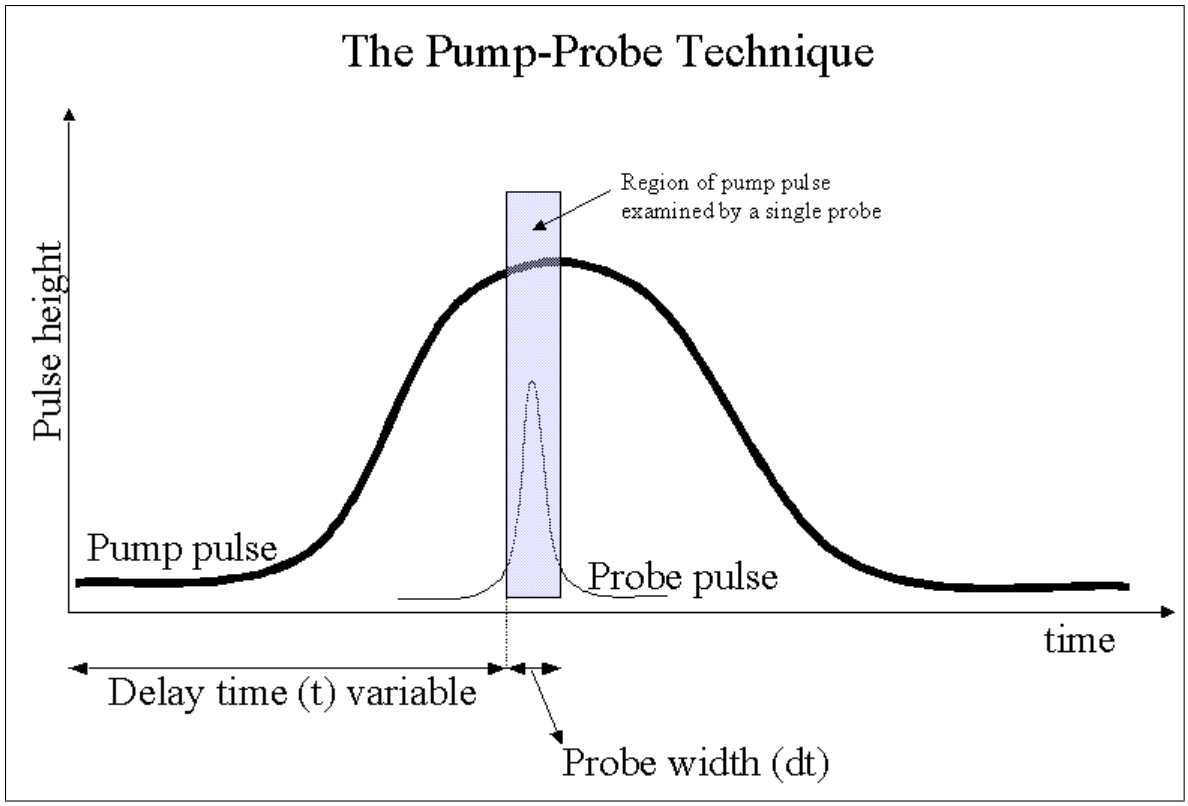

Figure 2-1: Cartoon of the pump-probe technique. The pump pulse moves the system out of equilibrium and the probe pulse measures the (nearly) instantenous state at succesive points during the process.

magnetization in the cores. These ferrite cores suffered from several serious problems most notably the large power requirements and even more problematic the destructive read operation. (The act of reading a bit reset the bit thereby requiring an immediate rewrite to follow every read operation.) Permalloy thin films (a family of Nickel-Iron alloys) looked to be a promising substitute for the ferrite cores since they could be formed with a uniaxial anisotropy and no demagnetization field in the plane, the two properties required to make a nice bit. This sort of particle could readily be modeled as a Stoner-Wohlfarth particle [29].

2.3 Modeling Magnetism

2.3.1 Stoner-Wohlfarth Model

To explain what is meant by a Stoner-Wohlfarth particle let us start with a single domain sample that has a uniaxial anisotropy and is immersed in a static external field. If we neglect other anisotropies we can write down an expression for the total energy per unit volume of such a sample.

$$W = -MH_x \cos\theta - MH_y \sin\theta + K \sin^2\theta \tag{2.7}$$

In this expression K is the uniaxial anisotropy constant, H_x, H_y, are the external field components, θ is the angle between the easy axis (the axis along which the magnetization would orient itself without an external field, assumed to be along x) and the magnetization, M.

Taking the derivative of this expression with respect to theta and setting it to zero gives the equilibrium magnetization position.

$$\frac{\partial W}{\partial \theta} = MH_x \sin\theta - MH_y \cos\theta + 2K \sin\theta \cos\theta = 0 \tag{2.8}$$

Doing this again for the second derivative gives.

$$\frac{\partial W^2}{\partial^2 \theta} = MH_x \cos\theta + MH_y \sin\theta + 2K(\cos^2\theta - \sin^2\theta) = 0 \tag{2.9}$$

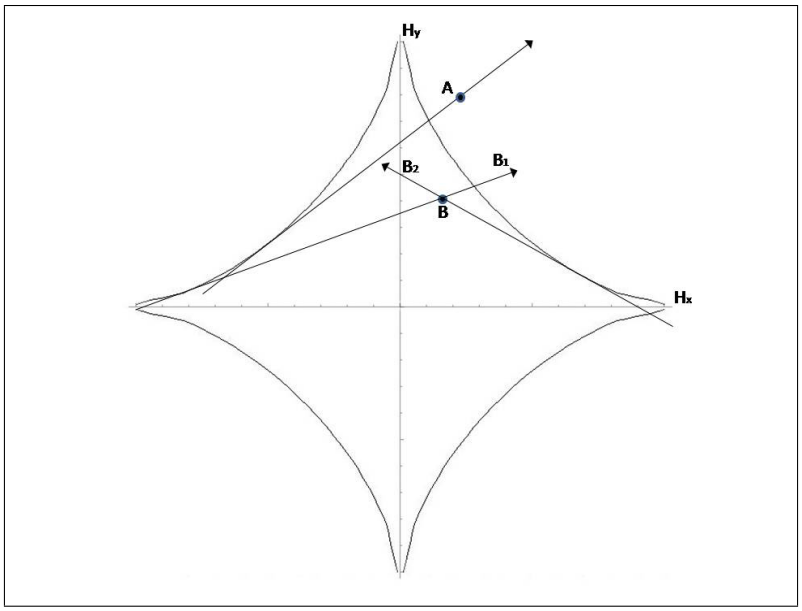

Figure 2-2: The Stoner Wohlfarth Asteroid. Point A outside the asteroid is a single stable state. Point B, inside the asteroid has two possible states B_1 nearly parallel to A and B_2.

The second derivative gives the transition points, where a stable state turns into an unstable state.

Combining both equations we can eliminate θ and get an equation in H.

$$(H_x)^{\frac{2}{3}} + (H_y)^{\frac{2}{3}} = \left(\frac{2K}{M}\right)^{\frac{2}{3}} \tag{2.10}$$

This equation is the Stoner-Wohlfarth asteroid, which shows the external field values for which the magnetization has a stable state. Figure 2-2 shows a plot of this equation. The value of $\frac{\partial W}{\partial \theta}$ is always tangent to the curve, (by virtue of the way the curve was derived,) so to find the equilibrium direction for any given external field we can draw a tangent to the curve that passes through the field point. The magnetization will then point along that tangent line as that is direction of maximum stability. So in the figure if the applied field is at point A (outside the curve,) the magnetization will lie along the arrow marked A. On the other hand if the applied field is weaker, lying at point B on the graph, the

magnetization can align along the arrow at B_1 (parallel to A) or it could align along the arrow at B_2. Apparently there are now two possibly stable states. In actual fact both states represent energy minima for the given conditions so they are both stable states under those conditions. However any deviation from the given conditions could cause the magnetization to flip from one state to the other. It is for this reason that the states with applied field coordinates inside the asteroid are considered unstable states. Imagine the magnetization is resting in the state B_2 and the external field is gradually increased. Even if nothing else happens to disrupt the magnetization state as the field is increased to a point lying on the curve, it must flip to state B_1 when the field strength is increased to a point outside the asteroid. At this point an interesting question presents itself. How does the magnetization get from state B_1 to state B_2? Another interesting question is how fast can it go from one state to the other?

The focus of the research rapidly grew toward answering the second question. Studies started to be published showing new kinds of magnetic reversals, referred to as coherent and non-coherent (or incoherent) reversals. One of the first works on the subject was that of Olson & Pohm [30] but all of the experiments follow the same general theme. The thin film was immersed in a static magnetic field oriented along the transverse (hard) axis of the film. A wire was used to switch the film along the longitudinal (easy) axis of the film and the same wire was connected to an oscilloscope to examine the induced current as the film switched. The inverse switching times were obtained from the traces and plotted as functions of the longitudinal field. In each case at a certain critical transverse field the slope of the graph changed rapidly. Although not immediately evident from Olson & Pohm's data further experiments showed the existence of three distinct modes, now commonly referred to as domain wall motion, incoherent rotation and coherent rotation. A completely coherent reversal is in some sense the opposite extreme of switching by domain wall motion and this can be neatly described the Landau Lifschitz equation which will be examined in more detail later. In the gray area between the two extremes are reversals which are a mixture of the two and are generally referred to as incoherent switching a phrase apparently proposed

by Gyorgy [31].

After this first real evidence of fast reversal processes that did not fit with domain wall motion Kryder and Humphrey [32] used a pulsed ruby laser to obtain 10ns temporal resolution of a magnetic sample being switched. The big advantage of Kryder's work was the fact that the domains (and therefore domain walls) were clearly visible in the images and so this can be considered as the first direct evidence of fast reversal. Several excellent sources are available to gather an overview of this period [33,34].

2.3.2 The Landau-Lifshitz equation

Earlier, reference was made to two questions stemming from the Stoner -Wohlfarth particle. How fast could the magnetization go from point A to point B, and how does it get from one point to the other? Of course the two questions are somewhat related in that how fast depends on the mechanism of the reversal. In the quasi-static regime the reversal is dominated by domain wall motion which is a relatively slow process. For reversal in the fast and ultrafast regime (~nanosecond time scales) domain wall motion is no longer sufficient. At these timescales the ideal reversal is a completely coherent reversal where all of the spins precess and come to rest at the new equilibrium position. We now turn our attention to how this might work. [1]

Since we want all of the spins to move in the same way it is sufficient to consider a single spin. The motion for a single spin is just a dipole moment in an external magnetic field. Letting μ be the magnetic moment of the single (electron) spin, H_{eff} be the effective field acting on that spin, and γ be the gyromagnetic ratio (~$1.76*10^7$/(Oe*s)) the equation of motion is:

$$\frac{1}{\gamma}\frac{d\mu}{dt} = -\mu \times \overrightarrow{H}_{eff} \tag{2.11}$$

The right hand side of the equation is the torque acting on the spin which, as a result

[1] This derivation is essentially the same as Landau and Lifshitz but can be found in most books that discuss magnetization dynamics. This follows the work of 35 and 36

of the cross product, is always perpendicular to the plane containing μ and $\overrightarrow{H}eff$, which describes a precession of μ about $\overrightarrow{H}eff$. Since together all of the spins in the sample make up the magnetization, we can rewrite the equation with $\overrightarrow{M}$ in place of μ to get

$$\frac{1}{\gamma}\frac{d\overrightarrow{M}}{dt} = -\overrightarrow{M} \times \overrightarrow{H}_{eff} \tag{2.12}$$

By itself this is not an adequate descripition however since the magnetization $\overrightarrow{M}$ has no way to relax and come to equilibrium aligned along effective field direction $\overrightarrow{H}_{eff}$which it must eventually do. To accommodate this, a phenomenological damping term is added to the equation, which serves to damp the precession and allow the magnetization to align along the direction of the effective field.

The original form of this equation was put forward by Landau and Lifshitz in 1935. The original form was:

$$\frac{d\overrightarrow{M}}{dt} = -\gamma(\overrightarrow{M} \times \overrightarrow{H}_{eff}) + \frac{\lambda}{Ms^2}\overrightarrow{M} \times \left(\overrightarrow{M} \times \overrightarrow{H}\right) \tag{2.13}$$

The problem with this particular formulation for the damping factor is that it is inappropriate if the damping parameter is large. In that case the frequency of the precession becomes abnormally large. Another formulation of the damping term was introduced by Gilbert in 1955 [35]. This equation is usually referred to as the LLG equation and is probably the most often quoted equation in dynamic studies of magnetics.

$$\frac{dM}{dt} = -\gamma\left(M \times H_{eff}\right) - \frac{\alpha}{Ms}\left(M \times \frac{dM}{dt}\right) \tag{2.14}$$

Although the LLG equation is a relatively straight forward looking equation, it should be pointed out that it is by no means a trivial thing to apply this equation to a realistic problem. A major problem is the sheer number of spins that are available in even the smallest physical system Even nanoclusters have thousands of atoms and most research is conducted on much larger scales with numbers on the order of Avogadro's number. Thus it is an n-body problem on a massive scale. The other major difficulty is in the effective field term. To this point not much has been said about the effective field but a word or two

about it is definitely required. In the derivation we simply took this term as the field applied to the dipole to find the torque but the question remains what exactly is the field? The $\overrightarrow{H}_{eff}$ term is the sum of all of the fields acting on the dipole. Obviously this includes any external fields but less obvious is the contribution of all of the other dipoles in the system. The calculation of the effective field from the other dipoles is one of the main difficulties in using the LLG equation to evaluate any realistic system. Those same interactions though are at the heart of magnetism so it is absolutely necessary to include them in one form or another. This is where most of the effort (and computation time) in modeling and computer simulation work is taken up - in calculating the $\overrightarrow{H}_{eff}$

With the concept of a coherent reversal firmly established both in theoretically and experimentally the ever-present question of 'how fast?' comes back again. This time however it is clear that how fast is not just a question of the switching pulse speed. The dynamics which lead to the coherent reversals are governed by several variables. Simulation work has shown that the fastest reversals are not solely achieved on the basis of the fastest pulses [36, 37]. The damping parameter and the demagnetizing field (wrapped up in the effective field term) both contribute to the dynamics. Controlling the shape of an excitation pulse can lead to faster, more stable switches [38] . In addition to the shape of the pulse one would expect that the degree of damping plays a significant role in the amount of magnetization ringing. The question of how the surface morphology of a film affects the damping however is still an open question.

Chapter 3

Experimental Setup

3.1 Overview of the Apparatus

The following details the experimental setup. It is an overview of the entire apparatus that was used and is given in three parts, the laser source and consequent electronics, the vacuum chamber and sample holder, and the detection setup. Details of the individual parts and their specific functions are given later as appropriate.

Figure 3-1 shows a schematic of the entire setup. The laser source was a laser diode pumped, mode locked, Titanium-Saphire laser, (a Tsunami laser from Spectra physics,) that produced ~100fs laser pulses with a repetition rate of 800 kHz. The wavelength of the laser was tunable around 800nm with a nominal power output of 1mW (the laser actually produces two beams one with a much higher power output and repetition rate but that beam was not used.) A beam-splitting cube was placed near the output window of the laser so that a portion of the beam could be used as a trigger for the electronics. The trigger portion of the laser was guided through an optical chopper, which ran at 800 Hz thereby producing a 1 kHz trigger signal which was received by a high-speed photodiode. The voltage output from the photodiode was used as a trigger for a delay generator, which then produced a trigger signal for a high-speed pulse generator. A computer was used to control the delay of the delay generator thereby adjusting the signal window.

The vacuum chamber was designed around a six way cross. The front port was used for allowing the laser access. On the top was a floating BNC feedthrough for the excitation

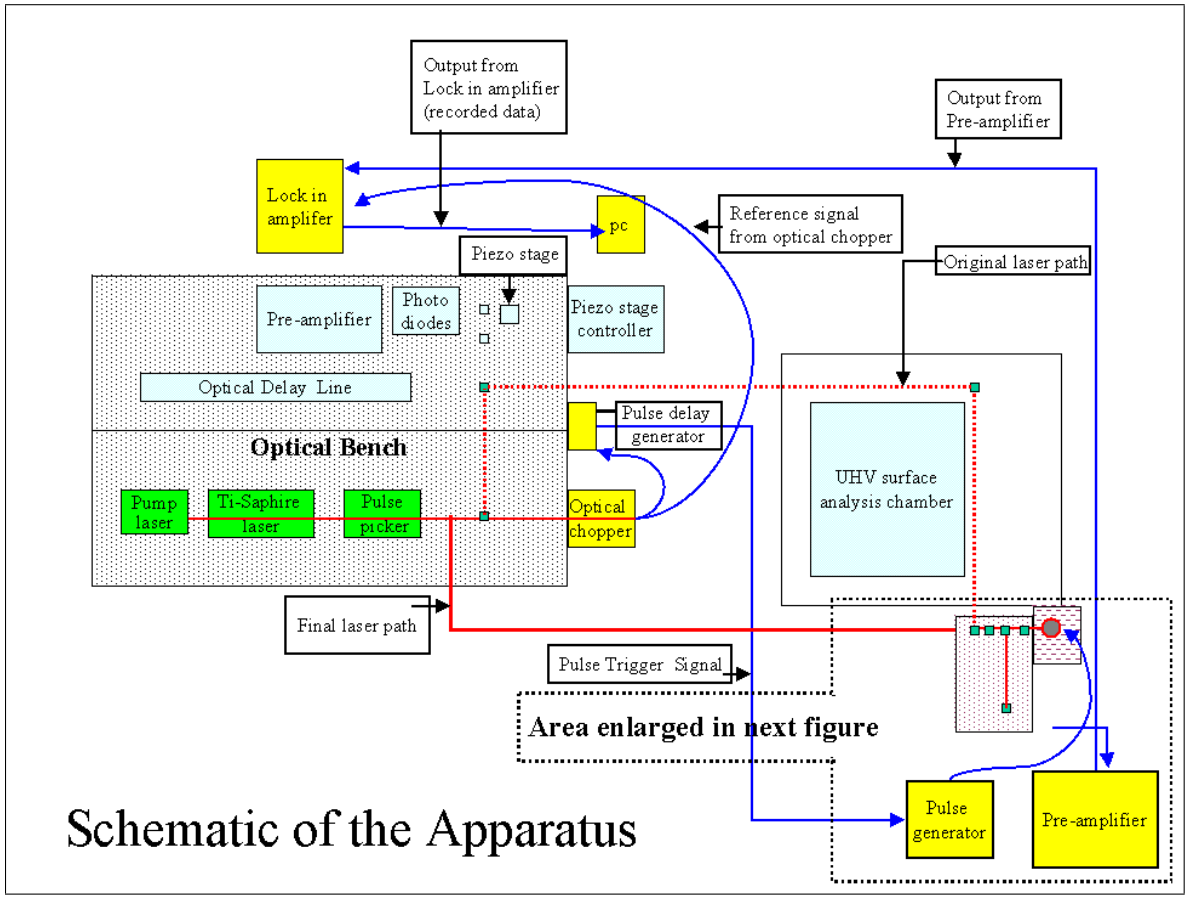

Figure 3-1: Schematic of the entire apparatus. The solid gray line shows the final beam path from the fs pulse-laser to the vacuum chamber. (The piezostage and preamplifiers on the left were not used in this setup.)

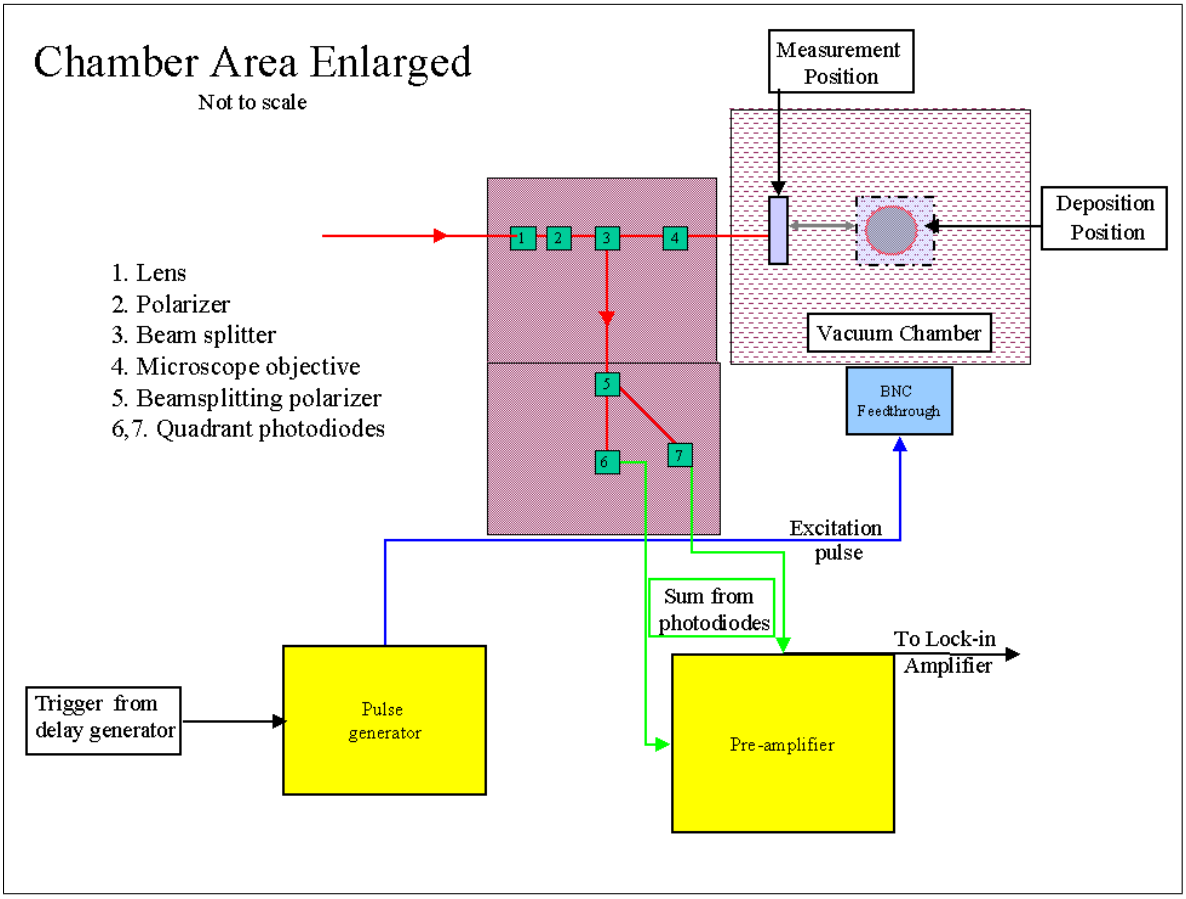

Figure 3-2: Enlargement of the vacuum chamber and relevant components. The chamber was set at ~10° to the vertical to reduce the reflections from the glass window.

pulse current. On the back was the translational stage control that was used in conjunction with the rotational control on the right to move the samples. The samples were positioned in either the viewing position which was as close as possible to the front window and facing forward or the deposition position which was centered in the chamber and facing down. On the bottom was the deposition source and water-jacket. The deposition source was a Permalloy pellet, contained in an alumina crucible, and heated by a tungsten basket filament. On the left was the connection to the turbo pump and the pressure gauge. The pressure gauge was a thoriated iridium filament gauge housed in a four way cross. This replaced a cold cathode-penning gauge, which was used in the initial stages of the experiment.

Figure 3-2 gives an enlarged view of the optical bench and chamber. The main group of optics was located on a bench adjacent to the vacuum chamber. After being reflected from the main optical table that housed the laser, the beam was sent thorough a long focal length lens (120 mm) to help fine tune its position. The beam was sent through a calcite polarizer to produce a good quality s-state polarized beam, which was then split by a 50-50 beam splitter. The transmitted portion of the laser then entered a microscope objective (10x - 0.25 NA with a working distance of ~1cm) and was focused through the high vacuum window onto the sample. A beam spot of ~30 μm in diameter was readily obtainable based on imaging structures of known size. Although a smaller diameter would have been preferred the limitations of system, (in particular the thickness of the window and the placement of the sample,) made a smaller spot size impractical. After reflection off of the sample the laser was recollimated by the same objective and sent back to the beam splitter. Using the reflected fraction from the beam splitter this time, the laser was sent through a beam splitting polarizer (henceforth referred to as the analyzer) set at ~45 degrees. Photodiode detectors then detected the two emerging beams.

3.2 Details of the apparatus and procedures

There were a number of factors that came to light during the course of the experiment that effected the final working operation. This part discusses those parts of the apparatus that

need more explanation or that were changed along the way to make it all work.

3.2.1 The beam path

The final beam path was in fact the third choice of paths. A single mode polarization maintaining optical fiber was the first attempt at constructing a beam path. This failed due to the lack of intensity through the fiber. The second beam path, which is shown as a fine dashed gray line on diagram 3-2, was also found to be inadequate. Originally this beam path was chosen as matter of convenience since the optical path of the laser was easiest to intercept at that point. The problem with this optical path was that it required having optical elements on four independent surfaces. Even minor vibrations became amplified as a result of the number surfaces moving independently of one another. The third and final beam allowed for all of the optical elements to be assembled on only two surfaces. The optical table that housed the laser, which was vibration isolated, and a threaded aluminum breadboard, which was not vibration isolated,(shown in figure 3-3 without the lead blocks). To decrease the amount of vibrations affecting the breadboard, the feet were placed on rubber pads, and several blocks of lead were placed on top. This relatively simple solution was enough to keep the vibrations to a manageable level.

Another problem with the beam path was unwanted reflections, most notably reflections from the chamber window. Since reflections inherently change the polarization state of the beam it was necessary to limit the reflections as much as possible. Additionally the beam needed to be as near to normal incidence as possible to maximize the polar Kerr signal. Initially this meant that it was nearly normal to the chamber window as well. Reflections from the sample and the chamber window (see figure 3-4) were both passed to the detector system, which degraded the overall signal. A simple solution to this was found by adjusting the angle of the chamber. By tilting the entire chamber ~10 degrees off the vertical and rearranging the sample holder to ~10 degrees in the opposite direction, the laser was able to contact the sample at normal incidence while reflections from the chamber window were eliminated.

Figure 3-3: Picture of the optics in front of the vacuum chamber. Lead blocks (not shown) were used to help stabilize the optical table.

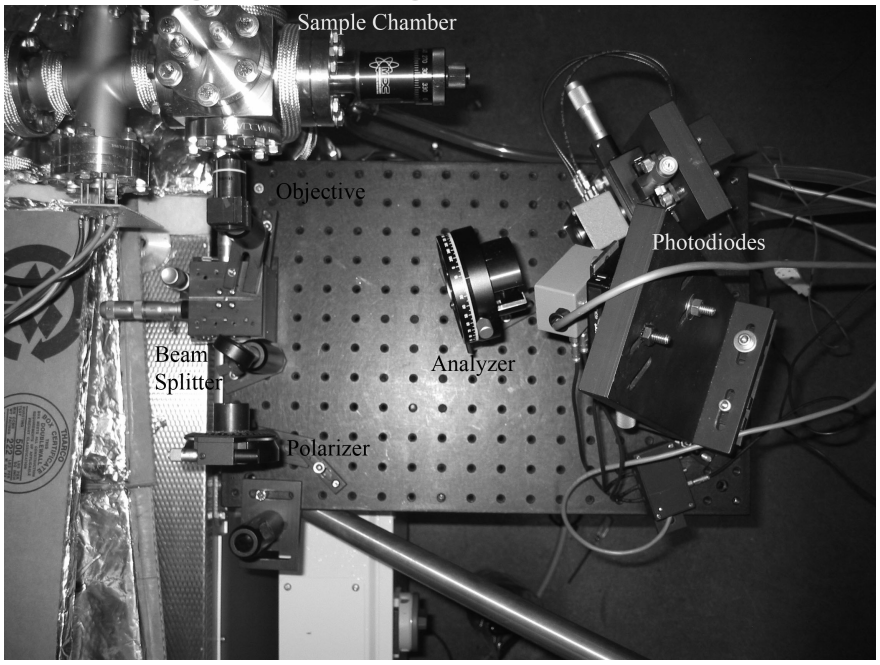

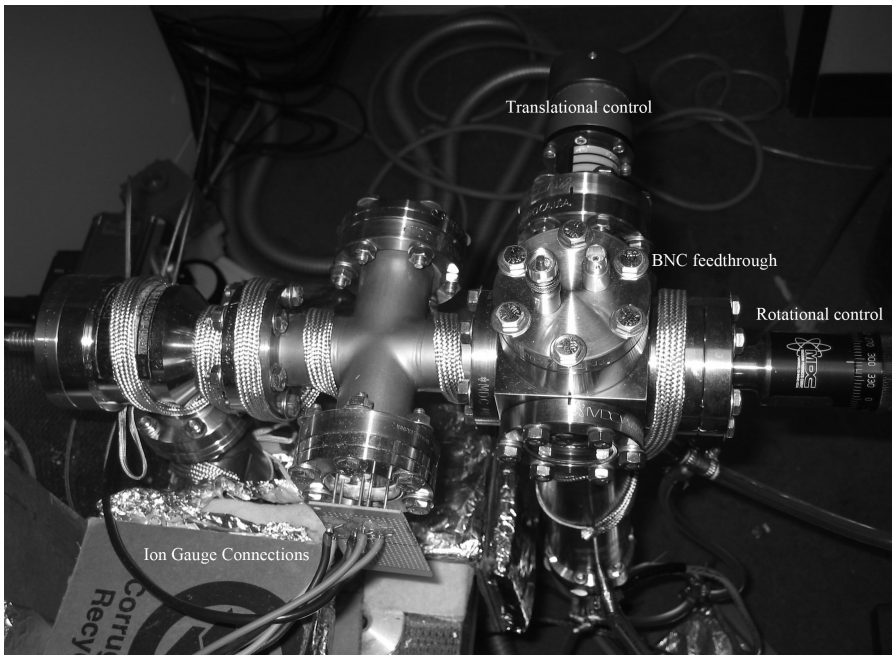

Figure 3-4: A front view of the vacuum chamber setup. The pump connection was made through the valve on the left. The braided band is a heater tape.

3.2.2 The polarization state

The actual state of polarization was not in fact a true s-state. Because the beam was necessarily reflected from a number of surfaces, all of which contributed to small (but constant) changes in the polarization state, the initial polarization was not exactly s-state. The polarizer was adjusted (as well as adjusting the position of the photodiodes) to help balance the initial signal from the photodiodes. The adjustment however was small, no more than three degrees, and the actual orientation of the polarization state has no bearing on the polar Kerr signal in any case.

3.2.3 Depositon conditions

The deposition was done by thermal evaporation of nickel iron alloy, more commonly known as Permalloy. The term Permalloy covers a family of Ni-Fe alloys of approximately $Ni_{80}Fe_{20}$ composition, in our case the composition was $Ni_{81}Fe_{19}$. A Leybold turbo pump backed by a rotary oil-roughing pump was used to evacuate the chamber. The system was connected through a side port on the pump so that the existing connections did not have to be disturbed. This was found to be a satisfactory solution although it likely contributed to longer pump down times. The ultimate pressure that could be reached, with a baking out at 125 C was ~10^{-9}mbar, however this was found to be impractical, (taking more than a week.) In practice the system was allowed to pump down overnight which brought the pressure down to ~10^{-7}mbar, then the filament was gradually heated up by applying increasing amounts of current to the filament (to a maximum of ~50 A.) After another day (or more depending on the nature of the work that had been done on the system) the pressure was ~10^{-8}mbar and the filament and crucible were well outgassed. This procedure allowed the pressure to stay in the 10^{-7}mbar range during the deposition. The deposition was initiated by bringing the current up to 70A and waiting for the pressure to stabilize at that current. Then the sample was moved into place above the source. Deposition times varied depending on the thickness of the film required. An average deposition time was 30 seconds at 70A of current that resulted in film thicknesses on the order of 20 nm. In

the initial set up the filament was connected to two solid copper conductors of an electrical feedthrough by two stainless steel clamps. Although this appeared to be satisfactory at first, after continued use it was noted that a thin black tarnish had built up on the stainless steel. This was caused by the heat of the filament over an extended period of time. During the same period it was noted that many of the films that were grown would not produce any temporal magnetic signal (although they still showed a magnetic response in the static moke setup.) Although not the only factor it is reasonably certain now that contamination from impurities in the stainless steel were a significant contribution to the lack of response form the early films. A new set of clamps was designed using an RF feedthrough. The RF feedthrough was comprised of two hollow copper conductors. Two copper clamps were silver soldered to the vacuum side and cooling water was circulated through each side using a smaller diameter tube fitted on the inside of each copper conductor.

3.2.4 Samples

An AFM image of one of the microcoils is shown in figure 3-5a, the internal gap was ~$50\mu m$ for all of the coils used. The samples were all evaporated on to prefabricated microcoils a schematic of which is given in figure 3-5b. To make the microcoils the substrates, 0.50 mm thick glass, was cleaned in a piranha solution ($3H_2SO_4$ - $1H_2O_2$) for 15 minutes. They were then removed, dried with N_2, and placed in a high vacuum sputter chamber. After obtaining a pressure of 10^{-7}mbar a thin layer of chromium (~10nm) as an adhesion layer and a thicker layer of gold (~250nm) were deposited under argon. This was all done at the University of Alberta's Nanofab facility. The (100x100)mm^2 substrates were then cut into smaller squares, ~(20x20)mm^2, then optical lithography and chemical wet etch were done at either UBC's AMPEL facility or the Nanofab facility depending on the batch. (The samples that comprise the final data were all done at UBC and were in fact all from a single exposure to help maintain consistency.) In the first attempts at producing films it was found that the resistance of the coils dropped significantly (10% or more depending on the thickness) after depositing the permalloy. This was largely attributed to the metallic

permalloy short circuiting the coil. Even though the permalloy was much thinner and has a lower conductivity some of the current still went through. To avoid this the later batches of coils were not stripped after the chemical etch. This left a thin layer of the photoresist on top of the coils providing some electrical insulation between the coil and permalloy film. Using this procedure the resistance was found to drop by only ~1% or less for the measured films. [1] A picture of the sample holder as seen through the chamber window. The microcoils were connected by the two spring clips.

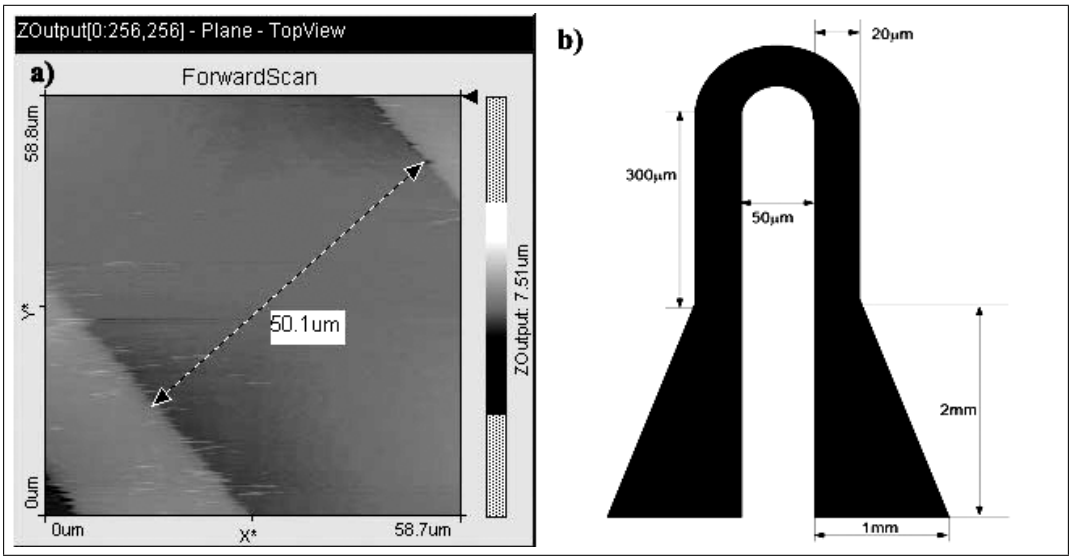

Figure 3-5: a) An AFM image of a bare microcoil. As shown the gap between the two wires is ~$50\mu m$. The width of each wire was ~$20\mu m$. b) A schematic of the microcoils used.

3.2.5 The excitation pulse

[1] The insulation provided by the photoresist was not perfect and the photoresist layer did occasionally break down producing a sudden drop in the resistance. A thin layer of insulating material, such as SiO_2, would have been more effective but was impractical to fabricate at this point.

High-speed current pulses travelling through the micro coil excited the magnetic films. The pulse generator was set to produce 4ns pulses with a peak voltage of 45 V. Given that the resistance of the system was ~50 Ω, (which was chosen to match the impedance of the cables to avoid reflections,) the pulse current was approximately 1A. Two spring clamps fashioned from a vacuum compatabile Be-Cu alloy made the connection to the coil. A picture of the sample holder as seen through the window of the chamber is shown in figure 3-6.

A section of vacuum compatible coaxial cable connected the clamps to the BNC feedthrough which was a two connector floating type. As it was first connected the circuit ran from one feedthrough connector, along the inside of the cable to the coil, then back along the shielding to the second connector. On the outside a modified BNC cable carried the pulse from the pulse generator in the same fashion. This mimicked the setup that has been used successfully on the optics bench in the past. Unfortunately that was not the case with this set up as connection in this fashion led to a large amount of interference. The system that did finally work was to ground the out going pulse to the chamber. In this case the pulse traveled along the inner conductor to the coil, and was then grounded to the sample holder after transiting the coil. The shielding of the coaxial cable was also grounded to the chamber. Using this connection method produced no measurable interference. The field strength of the pulse was estimated to be ~100Oe using a mathematica code which is given in appendix 2 as well as a plot of the estimated field distribution.

3.2.6 The photodiodes

The photodiodes that were used to detect the signal were actually a matched pair of quadrant diodes as seen in figure 3-7.

Although it wasn't done in this experiment the quadrant diodes allow for the detection of all three magnetization components. This detection unfortunately requires a very close focus with the sample, (or a very broad beam), in order to achieve large incident angle which was unobtainable in the current configuration. In future variations it may be possible to arrange the objective lens inside the vacuum chamber so that the angle of incidence is sufficiently

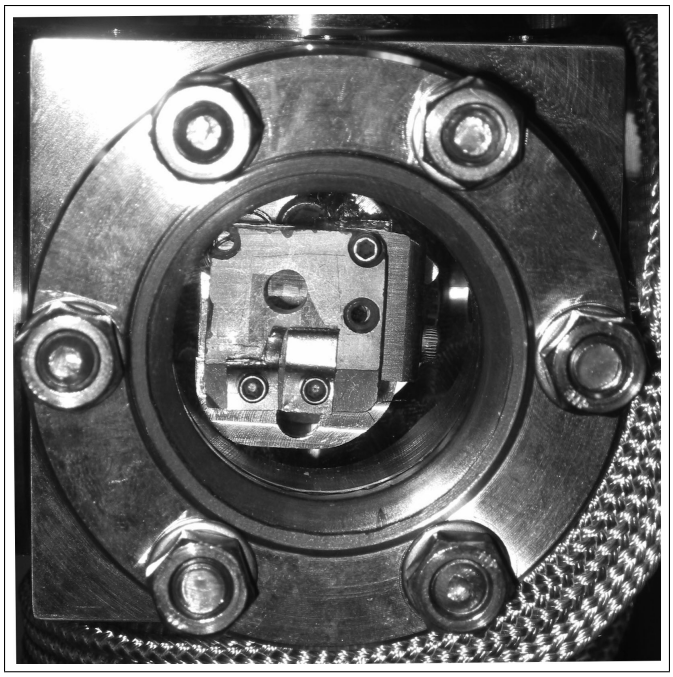

Figure 3-6: A picture of the sample holder as seen through the chamber window. The microcoils are connected by the two spring clips.

large to observe all three components. Use of the two-diode system however was still useful in that it increased the signal size. A traditional static magneto-optical microscope general uses only one diode and two (nearly) crossed polarizers. Any change in polarization is converted to a change in intensity. Using the two diodes and beam splitting polarizer at the analyzing end doubles the relative signal strength while simultaneously eliminating much of the background scatter. Any rotation of the polarization causes one of the two components of the polarization to decrease and the other to increase. This corresponds to an increase in the intensity in one diode and a decrease of equal magnitude in the other diode. Subtracting the two signals doubles the size of the change while simultaneously removing any components that remain unchanged. It should be noted that although this setup does allow for a removal of ambient light from the measured signal it was still found useful to keep the diodes as dark as possible. This was achieved by turning off the room lights and covering the diodes with a box.

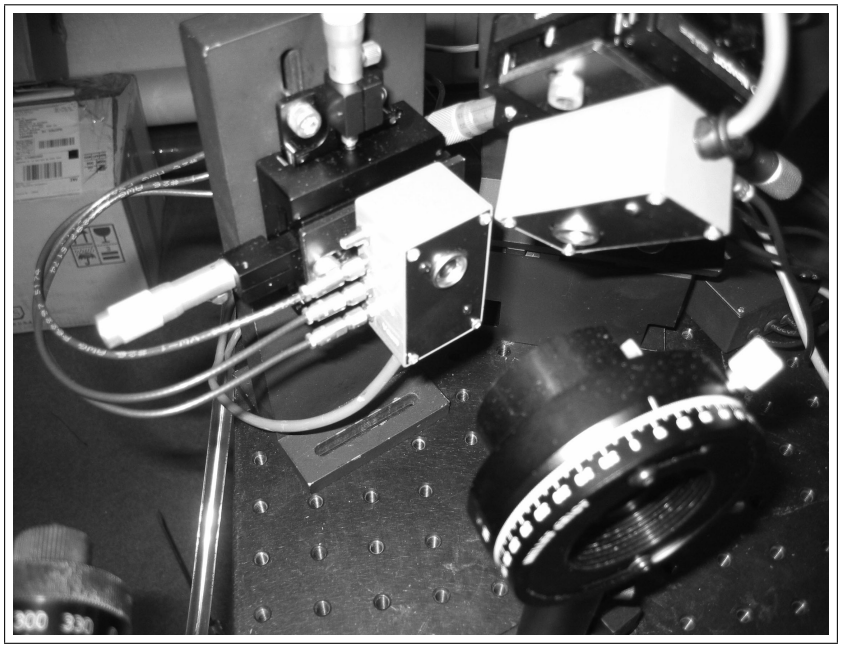

Figure 3-7: A picture of the photodiodes used along with the beamsplitting polarizer. During the measurements the diodes were covered to prevent stray light from reaching them.

Chapter 4

Results

To confirm the apparatus was working correctly a number of measurements were made on a Yttrium Iron Garnet (YIG) film prior to evaporation of any samples. These were readily comparable to scans done on the same film using a well established ex-situ system. Examples of this are given in Figure 4-1 and 4-2 and not surprisingly there is excellent agreement between the scans. It should be pointed out that although the y axis is arbitrary the same amplification parameters were used for both scans to allow for a comparison of the relative strength of the two signals.

After confirming that the setup was working films were produced and measured. The first films to show any response were done sequentially; a deposition followed by a measurement then another deposition and so on until the film no longer showed any response. Necessarily the thicknesses quoted are approximate, based on the measured deposition rates. Figure 4-3 shows the best of this set of scans with a damped sine wave superimposed over the peaks as an aid to visualization. The scans of these films were done with a 100 ps resolution but this was found to be too coarse to properly resolve the precession. The next series of scans more properly resolved the precession by using a 10ps resolution. These scans are shown in figures 4-4, 4-5, and 4-6. Each of these films was evaporated, dynamically scanned, hysteresis loops measured, and then removed for AFM measurements. This allowed for confirmation of the observed behavior and the predicted thicknesses as well as imaging of the surface structure.

Each of these films showed a good dynamic magnetic response and relevant data for each film is given in Table 4-1. The films were produced in the order of decreasing thickness

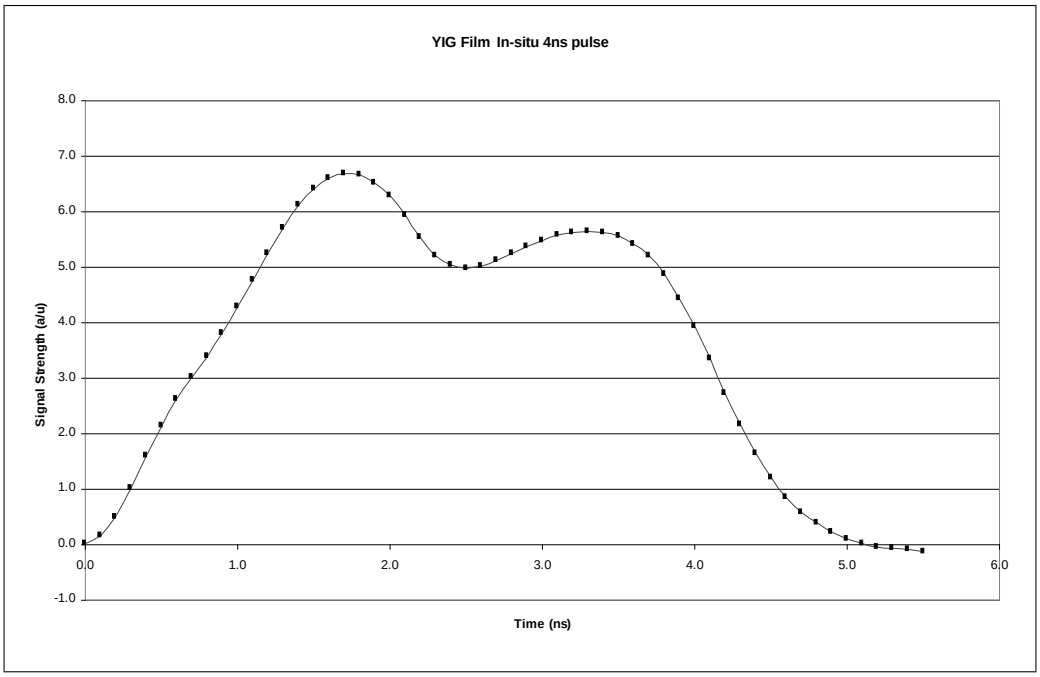

Figure 4-1: In-Situ measurement of the standard YIG film. The signal is from a 4ns pulse through a microcoil.

with the thinnest film (Film 1) being the final sample. (This final sample was made in two steps as the first evaporation was too thin to produce a magnetic response from the equipment.). The thicknesses quoted for these films are based on averages taken from AFM measurements. To do this the AFM was centered over an edge of the film, so that the boundary between the substrate and film was clearly visible. Then an area of the substrate and an area of the film were chosen and the average height of each was calculated (by the software), the difference between the two heights has been given as the film height. The resistances refer to the resistance of the coils as measured from the BNC feedthrough terminal. The initial resistance was measured as the sample was being installed in the chamber to ensure a good contact. The connection was only acceptable if it was less than 15Ω and it was measured again after the chamber was evacuated. The resistance was never found to change after evacuation, or manipulation of the sample, indicating a robust connection through the spring contacts. As was stated earlier, problems had been seen with

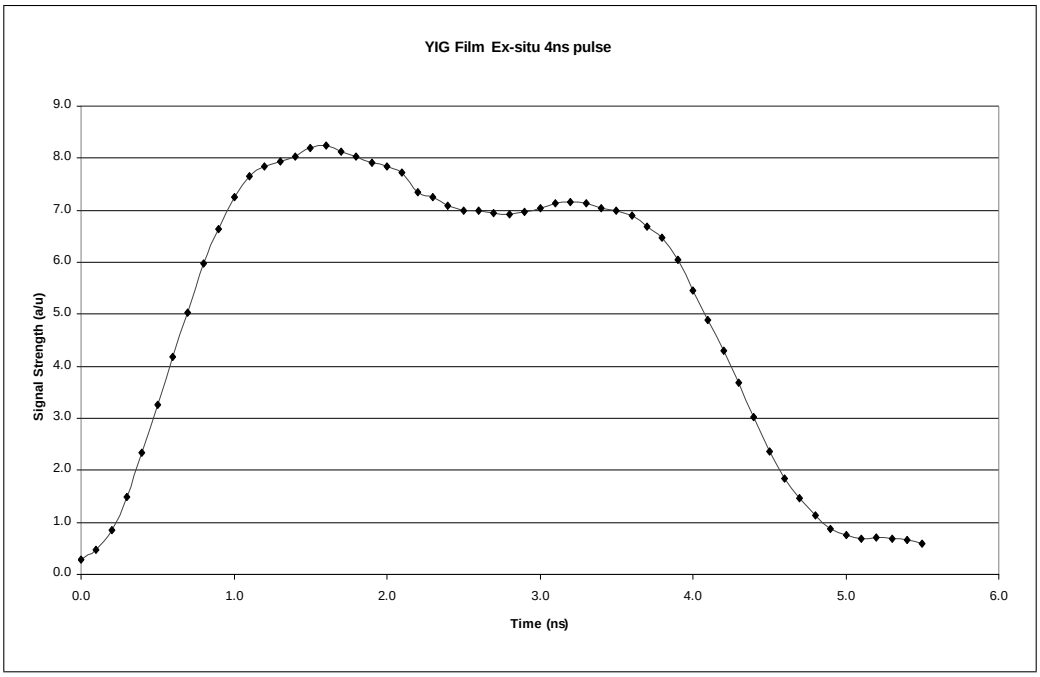

Figure 4-2: Ex-Situ measurement of the standard YIG film. The signal is from a 4ns pulse through a microcoil.

large resistance changes so monitoring the resistance after the deposition was necessary. For these three films a maximum change in resistance of 0.3Ω corresponds to a ~2% change in the resistance, which at 45 V corresponds to approximately a 4 mA change in current when the impedance matching is taken into account. The deposition power was measured using a Fluke clamp meter around the current input. In general a 70 A current was used although for the thinnest film a 65 A current was used in an effort to have more control over the thickness. Also the times represent the time that the samples were turned into the evaporant stream, in the case of film 1 this is the combination of 10 seconds in the first run and 5 seconds in a second run. The deposition pressures represent the median of the pressure during the deposition.

As mentioned above the hysteresis loops for the 9 nm, 18 nm, and 22 nm films were also measured. This was accomplished by arranging a pair of coils outside the chamber with the generated field oriented along the axis perpendicular to the plane of the film. A

Film	1	2	3
Thickness	8.8 ± 0.5nm	18.3 ± 0.5nm	22.3 ± 0.5nm
Initial Coil Resistance	14.4Ω	14.2Ω	14.6Ω
Final Coil Resistance	14.5Ω	14.3Ω	14.9Ω
Resistance Change	0.1Ω	0.1Ω	0.3Ω
Deposition Power	65A	70A	70A
Deposition Time	15s	20s	30s
Deposition Rate	0.59nm/s	0.91nm/s	0.74nm/s
Deposition Pressure	$6x10^{-7}$mbar	$3x10^{-7}$mbar	$5x10^{-7}$mbar

Table 4.1: Characterization and deposition information of the Films

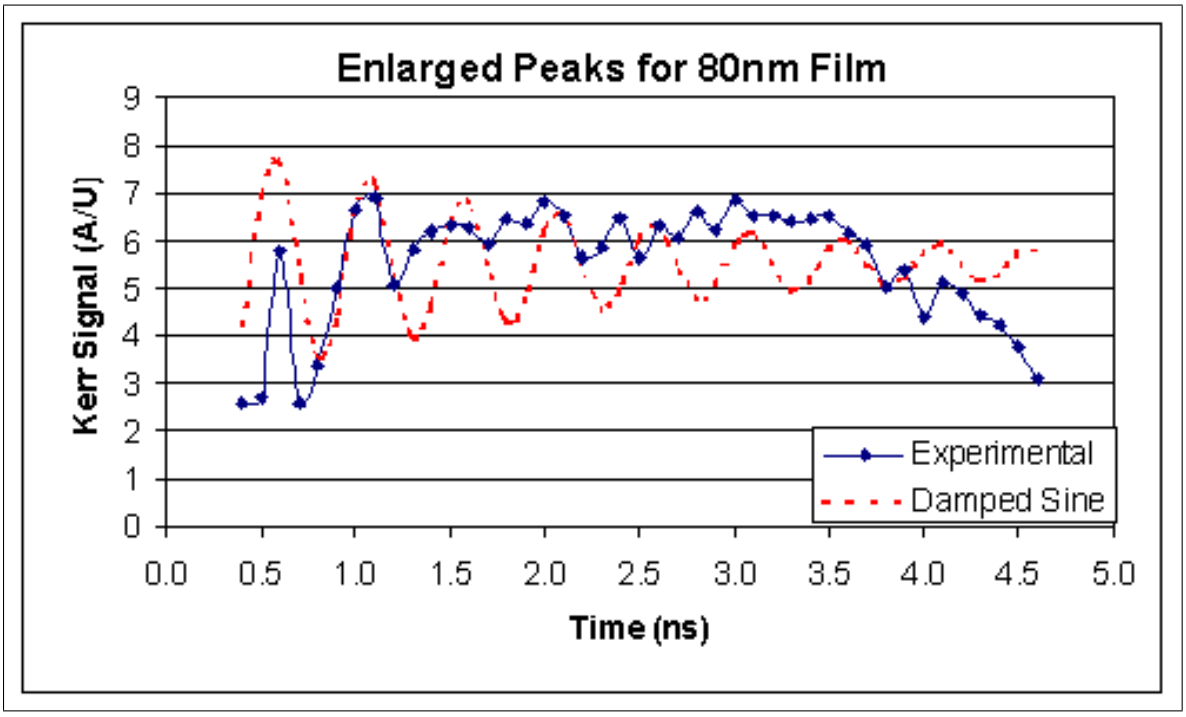

Figure 4-3: A dynamic scan of an 80nm thick film with a damped sine wave superimposed. The precessions in the film are poorly resolved but visible.

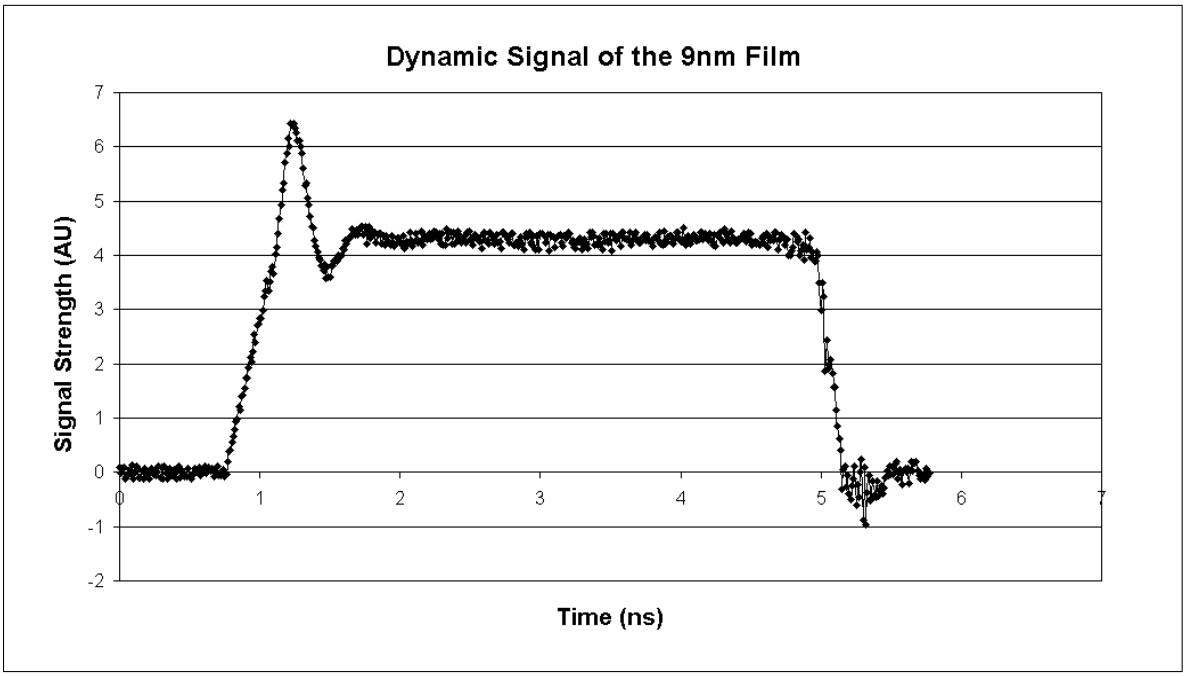

Figure 4-4: Plot of the entire scan for the 9nm thick film. The precession is abruptly damped.

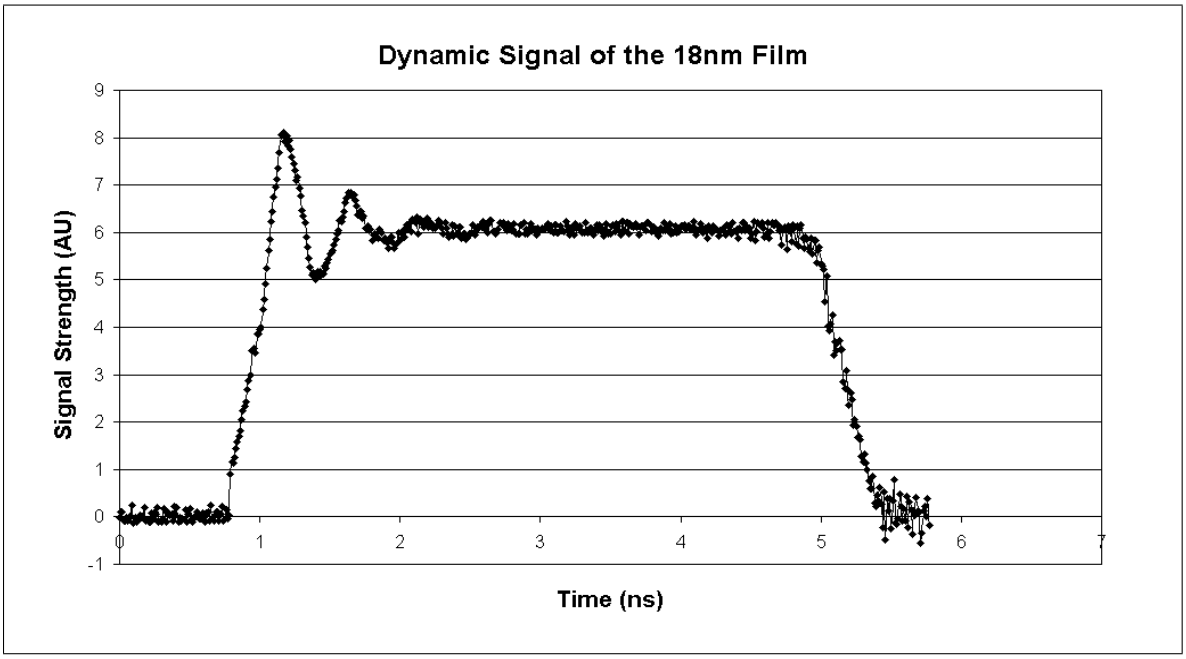

Figure 4-5: Plot of the entire scan for the 18nm thick film. The precession is lasts somewhat longer than in the thinner film

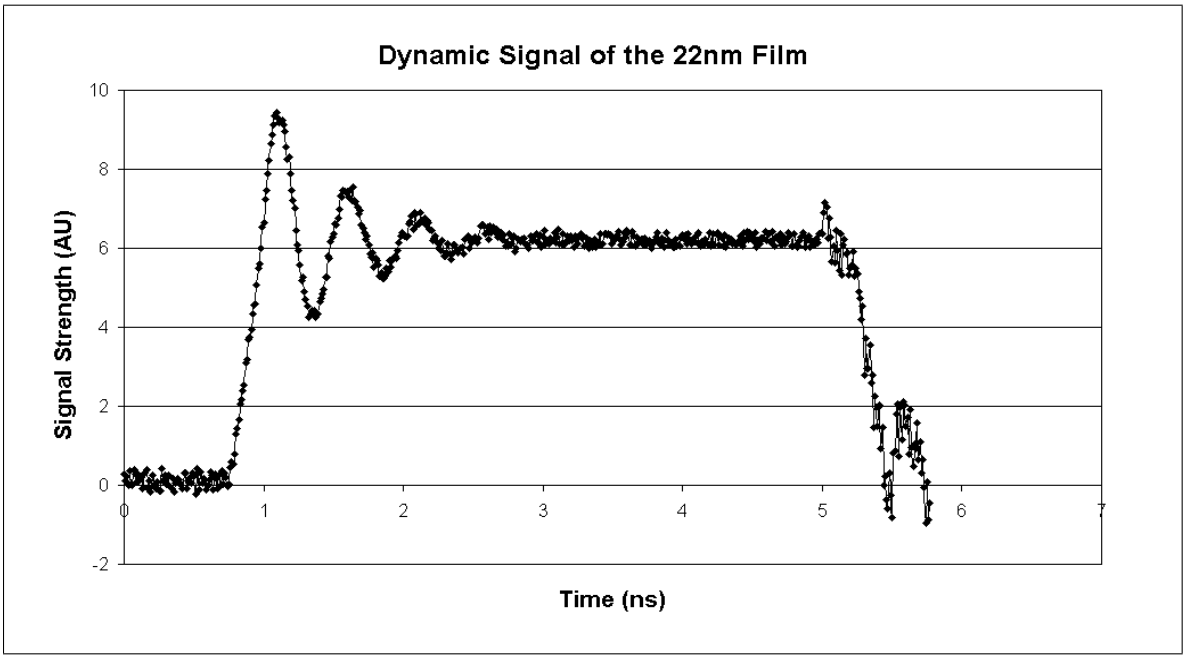

Figure 4-6: Plot of the entire scan for the 22nm thick film. The precession is long and well resolved.

current of 4A at a frequency of ~1Hz was used to generate the field. Figures 4-7(a), 4-8(a), and 4-9(a) show the hysteresis loops for each film on the left, on the right, figures 4-7(b), 4-8(b), and 4-9(b), are the AFM images of the corresponding films. Note that the vertical scale for the first AFM image, 4-7(b), is half that of the other two. Brighter areas represent topographical peaks.

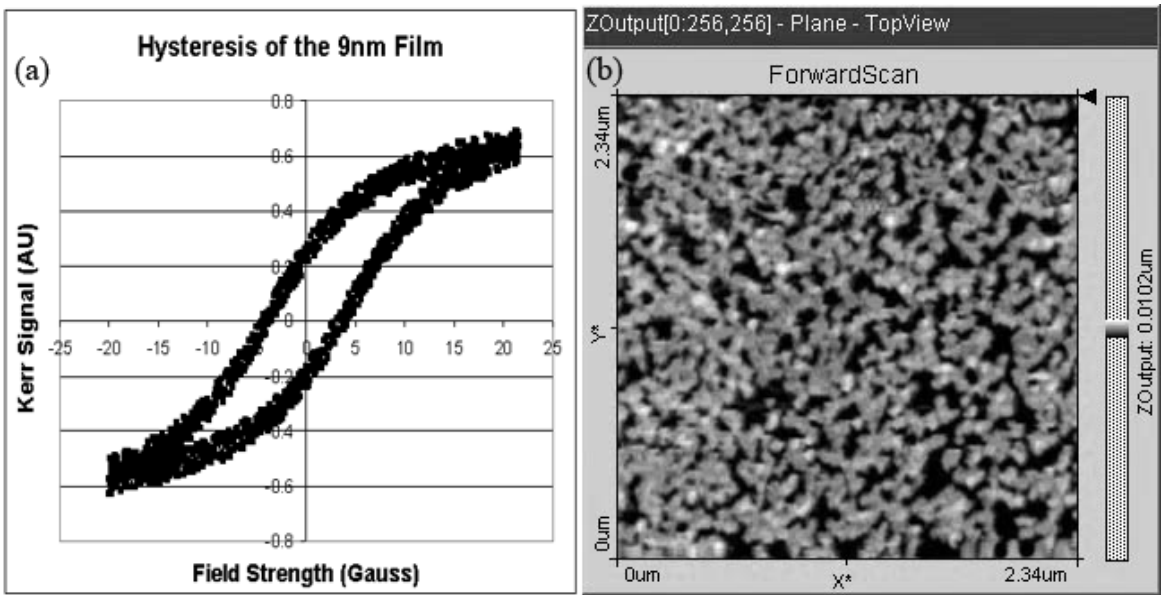

Figure 4-7: a) the hysteresis loop for the 9 nm film, b) the as scanned AFM image of the 9 nm film.

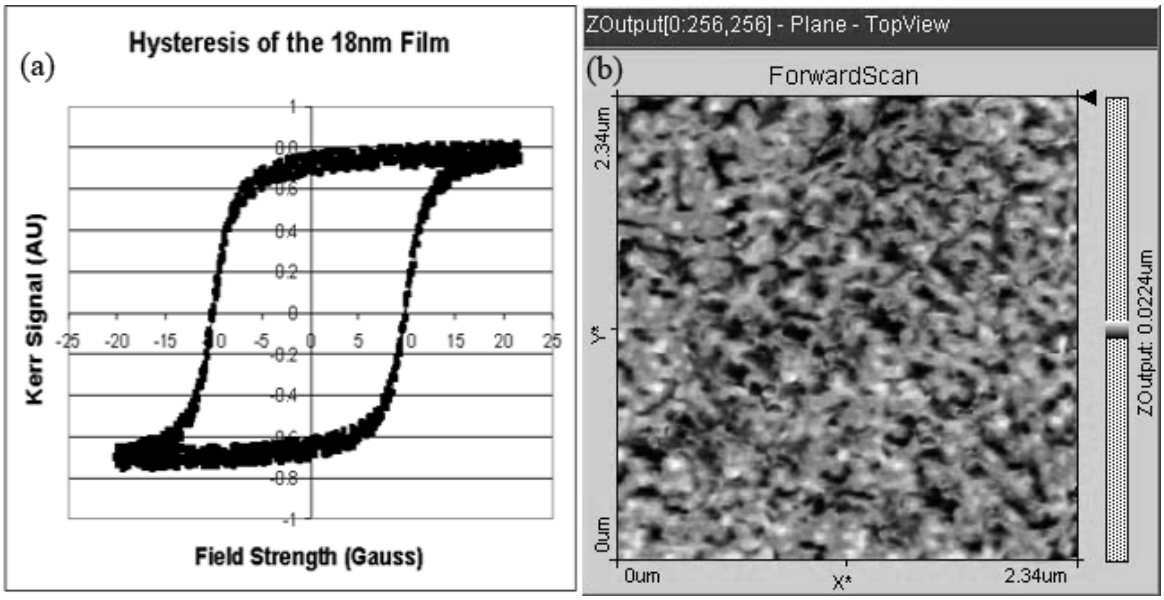

Figure 4-8: a) the hystersis loop for the 18 nm film, b) the as scanned AFM image of the 18 nm film.

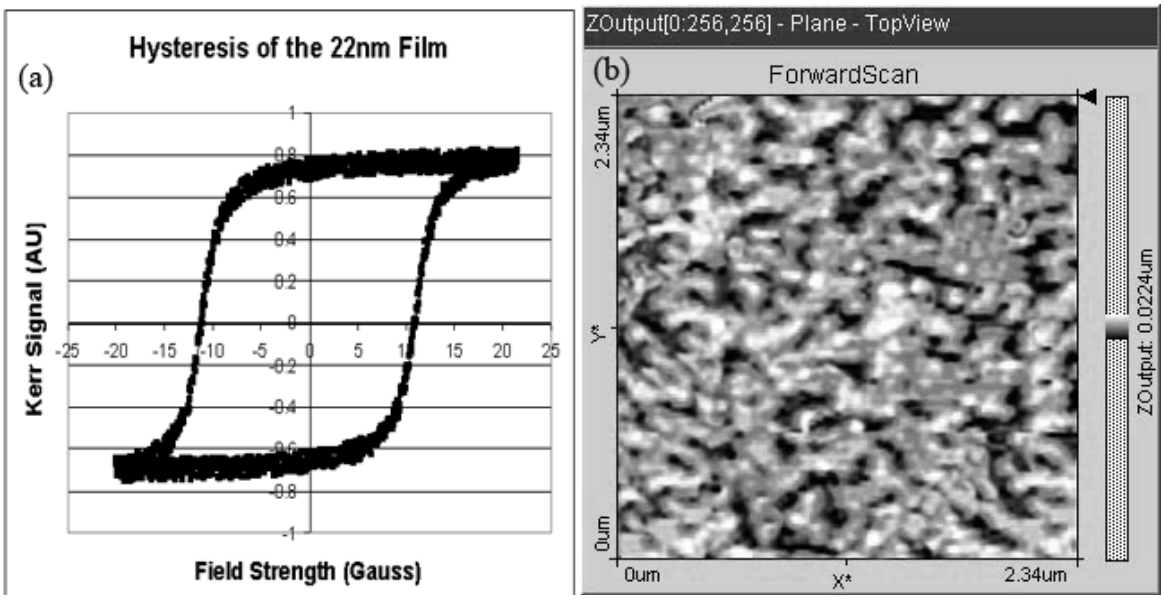

Figure 4-9: a) the hysteresis loop for the 22 nm film, b) the as scanned AFM image of the 22 nm film.

Chapter 5

Analysis

As shown in the AFM images (figures 4-7(b), 4-8(b), and 4-9(b)) all films investigated reveal the three-dimensional island growth mode, in which the surface structure is composed of Py islands separated by void areas. The sizes and separations of the islands are of a wide distribution, and no isotropic feature of the surface structure can be readily identified. To better visualize the surfaces 3-dimensional Matlab plots of the AFM images are given (figures 5-1(a)-(c)) and to obtain a quantitative view of the surface roughness the profiles of the AFM images are captured as shown in figure 5-1(d). The general trend is that increasing film thickness leads to larger vertical surface roughness. by correlating the brightness to heights. The root-mean-square (rms) roughness (i.e., standard deviations of island height) of the deposited films are measured 5.3 nm, 19.1 nm, and 21.3 nm for Py film thicknesses tPy=9 nm, 18 nm, and 22 nm, respectively. Note that the heights in figure 5-1(d) represent variations in the surface of each film and do not include any vertical offset. The quoted thicknesses include the vertical offset relative to the substrate. For the 18 nm and 22 nm thick films, since the average island height does not change drastically, the implication is that some type of continuous Py layer forms under the islands by means of percolation.

The examination of the (quasi) static data from figures 4-7(a), shows a typical hard-axis behavior indicating that the magnetization easy axis at this thickness range (9 nm) is in the film plane. With increasing thickness it can be seen that the shape of the loops change to square-like (Fig. 4-8(a)), indicating that the direction normal to the film plane becomes the magnetic easy axis. The origin of the perpendicular anisotropy is attributed to the larger surface roughness at this thickness. This is in agreement with a previous theoretical

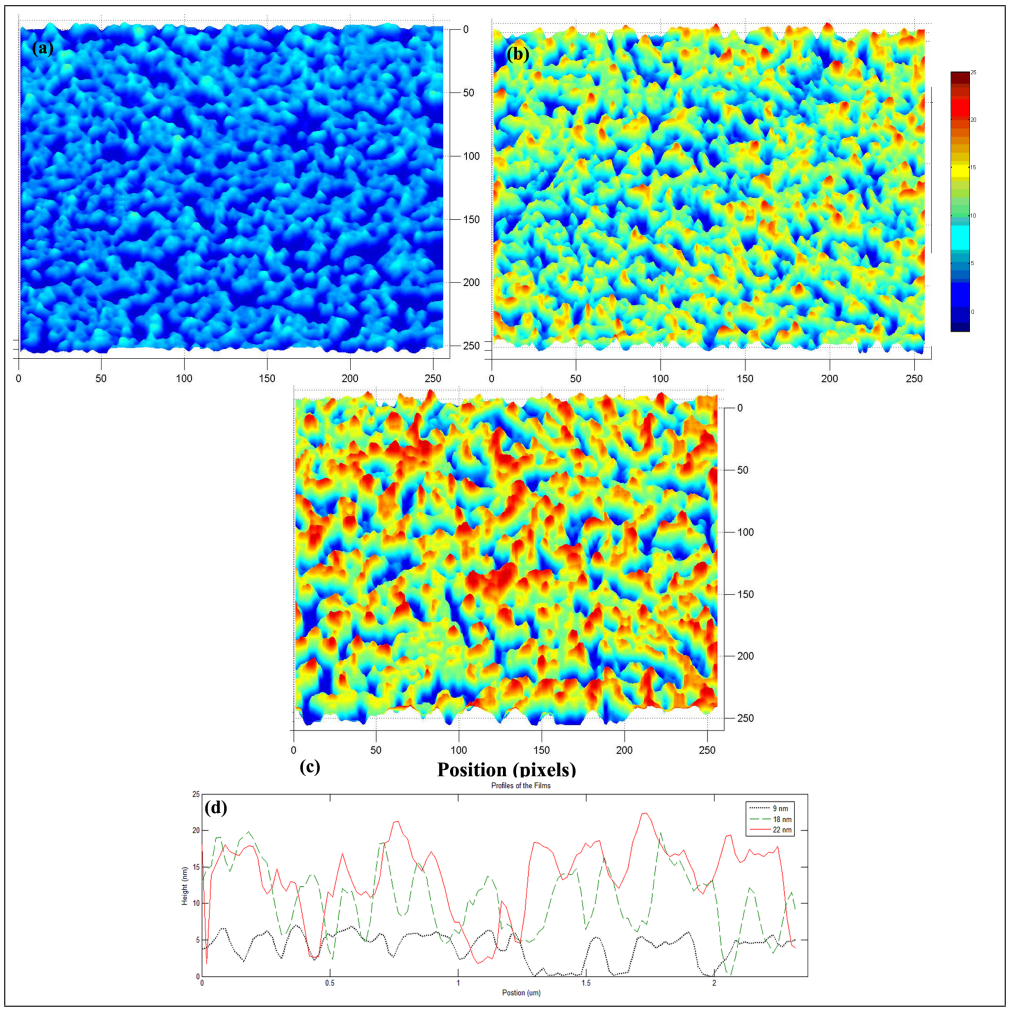

Figure 5-1: (a)-(c) show the three dimensional surface maps of the 9 nm, 18 nm, and 22 nm films respectively all done on the same scale (color bar at right.) Figure (d) is a plot of the profiles for each film taken along the midline of each AFM image.

study by Bruno [39], in which the surface roughness was expected to result in an effective positive dipolar surface anisotropy. The hysteresis loop measured for the 22 nm thick film (Fig. 4-9(a)), which has a slightly higher rms roughness compared to the 18 nm thick film, shows an increase in squareness and the coercive field, suggesting that the perpendicular magnetic anisotropy strongly contributes to the magnetization process .

The direct correlation of the surface morphology to dynamic magnetic properties is found in the time-resolved Kerr measurements. As already mentioned, the time resolved measurements were made by applying a magnetic field pulse along the direction of the surface normal. This field pulse brought the Py film systems out of equilibrium, therefore the detected magneto-optic signal results from the change in the out-of-plane component of the magnetization, (the Mz component of M.) Since the laser spot is focused to a beam spot of ~30 μm in diameter, the time traces of Mz correspond to the evolution of the magnetization in each film averaged over the area of the beam spot, an area of ~700 μm^2. Figures 4-4, 4-5, and 4-6 show the complete temporal evolution of Mz, measured on the 9 nm (a), 18 nm (b) and 22 nm (c) thick films respectively. The time traces reveal damped magnetization oscillations which result from the large out-of-plane excitation of Mz that developed in response to the rapid change of the external magnetic field and the three films appear quite similar aside from the rapid quenching of the precession in the thinnest film, (figure 4-4.) Figure 5-2(a)-(c) shows the same data truncated so as to better examine the precessions and now an interesting observation comes to light; the faster magnetic response of Mz as the thickness of the Py increases. For a thickness of 9 nm (figure 5-2(a)), the initial excitation decays very quickly leaving a smaller amplitude precession as time evolves, implying a strongly incoherent magnetization precession. With increased film thickness as in the 18 nm film (figure 5-2(b)), the dynamic response of Mz changes and an additional excitation peak appears at 150 ps. The fast initial response of Mz is, however, quickly suppressed by the following large amplitude precessional motion, which dominates the dynamics on a long time scale. The presence of the two excitation peaks suggests the formation of two magneto-dynamically distinctive regions within the film. As was hinted at earlier with AFM images,

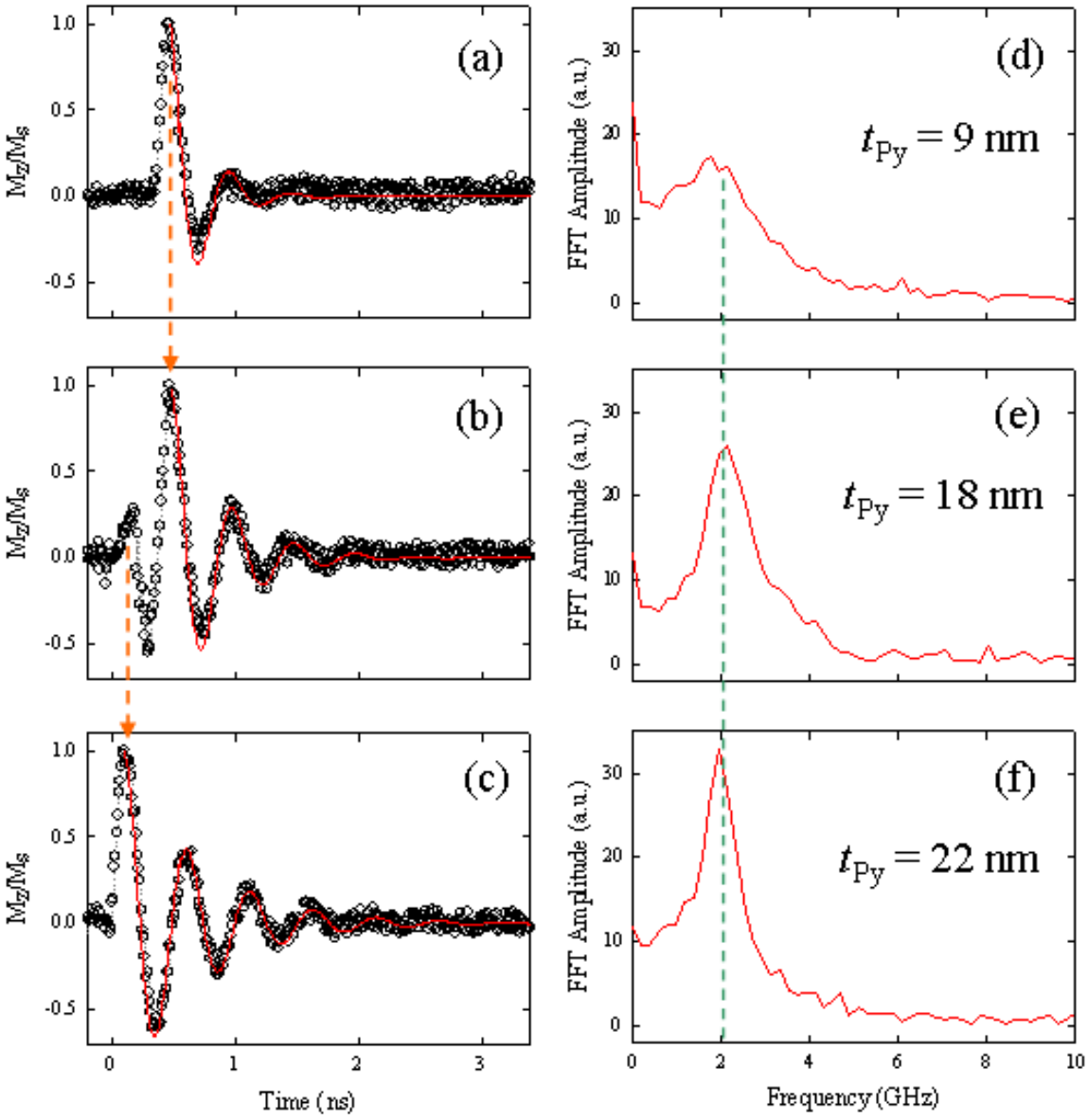

Figure 5-2: temporal evolution of Mz measured on (a) 9 nm, (b) 18 nm, and (c) 22 nm thick films as a function of delay time. The magnetic pulse begins at 0 ns. Open circles are experimental data, the gray line (red online) is the best fit using $e^{\frac{-t}{\tau}}$. On the right, (d)-(f), are the corresponding fast Fourier transformation (FFT).

the film growth is primarily island growth but with an underlayer forming by percolation. The magnetically non-identical Py layers can be associated with these two different regions of film. One in which isolated Py islands exist and another in which the islands have percolated to create connected Py clusters in an underlayer. It should be noted that this type of film growth is not the idealized Stranski-Krastanov (i.e., layer plus island) mode, where islands grow on top of the first complete layer. The initial fast magnetic excitation of Mz is attributed to percolated underlayer while the delayed precessional excitation involves the response of Mz only from the isolated islands at the surface. Consequently the contribution to the magnetization dynamics from the islands is expected to become less significant with increasing thickness of Py. This hypothesis is confirmed by the measurement at a thickness of 22 nm (figure 5-2(c)), in which the precessional response observed in the 9 nm Py film disappears while the coherent precession of Mz starts at 150 ps and is preserved above 2 ns. The precessional frequencies for different thicknesses of Py are extracted by fast Fourier transformation (FFT) of the time trace of M, as shown in figure 5-2(d)-(f). The FFT of the 9 nm thick film does not produce a sharp peak due to the sharp decay of the magnetization oscillation, nevertheless, a precessional frequency of ~2 GHz can be clearly identified. As the thickness of Py increases, the peaks in the FFT spectrum become sharper since there are more oscillations being analyzed, but no shift of the precessional frequency is found. This implies that the spatial inhomogeneities in the percolated underlayer and the surface island layer, significantly affect the time scale of the dynamic response of Mz but not the intrinsic precessional frequency. This is understandable since the precessional frequency is a function of the material properties and therefore has its origins in the compositional details of the film.

Another parameter describing the magnetization dynamics is the decay time, τ, of the precessional oscillation of Mz [40]. The values of τ are determined by fitting the time trace of Mz with a damped sinusoidal function of the form $\mathrm{M(t)=Mo\ e}^{\frac{-t}{\tau}}\ \sin(\omega t - \phi)$, where ω is the angular frequency of the precession mode and ϕ is the initial phase of the precession. The solid gray lines in figure 5-2(a)-(c) are the best fits to the data, giving the

decay times τ = 0.25 ns, 0.41 ns, and 0.60 ns for Py thicknesses of 9 nm, 18 nm, and 22 nm, respectively. It is found that the exponential decay, $\sim e^{\frac{-t}{\tau}}$, of the precessional amplitude follows the experimental data better than the nonexponential decay of the form $\exp\{(\frac{-t}{\tau_{3/2}})^{\frac{3}{2}}\}$ based on considerations of the surface roughness induced two-magnon scattering [41]. We also note that our experimental data suggests that the decay time τ increases as the rms roughness increases. This is in contrast to the theoretical prediction by Dobin et al. [41], in which the decay time is expected to decrease as the amplitude of roughness increases. This discrepancy results from the film growth mode in our experimental environment in which islands are grown on top of the connected Py clusters. Taking this into account, the relative contribution of the surface roughness to the damping becomes less dominant with increasing film thickness.

The effective damping constant α_{eff} is determined using the extracted values of τ [42]. For Py thicknesses of 9 nm, 18 nm, and 22 nm, α_{eff} reach the values of 0.32, 0.19, and 0.13, respectively. The α_{eff} values obtained from the experimental data are plotted in figure 5-3. These values are considerably higher than any reported damping constants of, for example, 0.015 and 0.018 for 50 nm and 204 nm thick Ni80Fe20 films [43,44]. With increasing thickness, α_{eff} drastically drops and above 50 nm thickness it approaches the lower values previously reported. The fit to experimental data reveals that α_{eff} follows a line inversely proportional to the film thickness, $\alpha_{eff} \propto \frac{1}{tPy}$. The $\frac{1}{tPy}$ dependence of α_{eff} clearly indicates that the significantly enhanced damping originates from surface effects, i.e. roughness.

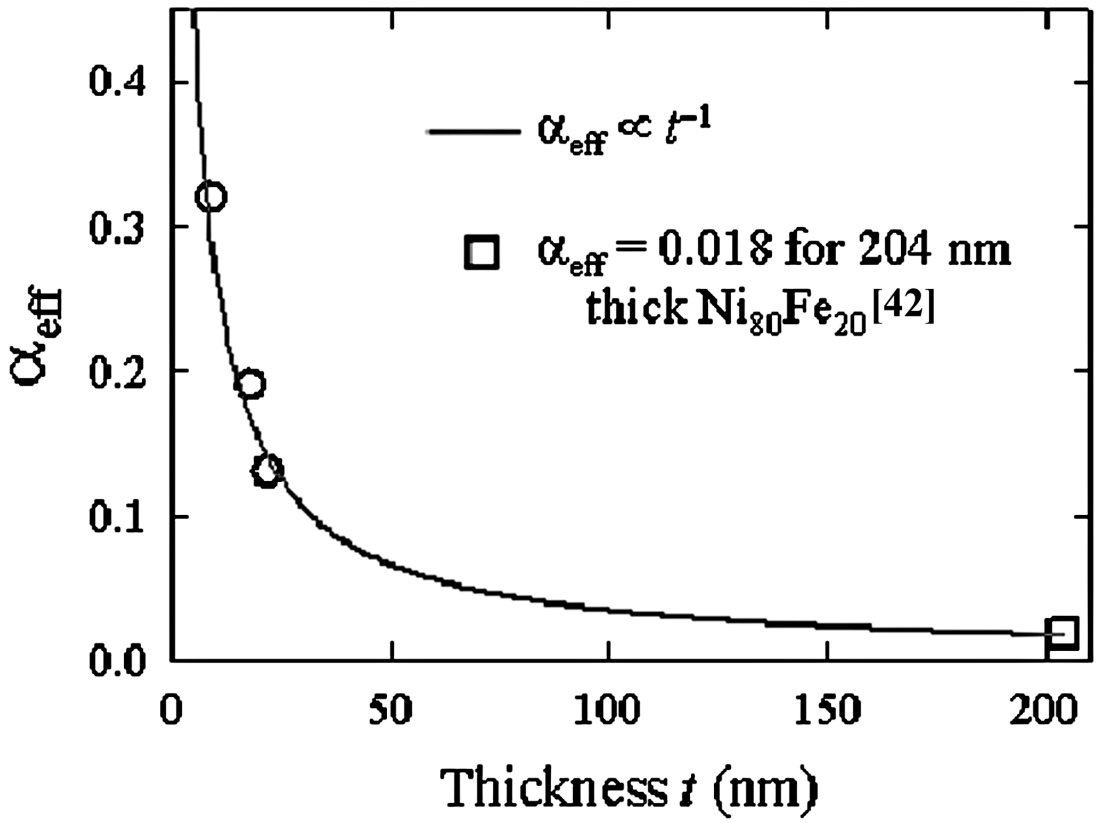

Figure 5-3: α_{eff} extracted from experiment (open circles) and best fit (gray line) using $\alpha_{eff} = \frac{1}{\omega\tau}$. The square symbol corresponds to the damping constant measured for 204 nm thick Ni80Fe20 film (J. B. Youssef [42])

Chapter 6

Conclusions

In conclusion, time-resolved magneto-optic Kerr effect (TR-MOKE) was used to study the in-situ magnetization dynamics of permalloy (Py) thin films grown under high-vacuum (~10^{-8} mbar) conditions. The picosecond time-resolved probing of the magnetic response allowed experimental determination of two important dynamic parameters, the precessional frequency and the effective damping constant, α_{eff}, in the magnetic thin films. The two parameters show distinctively different film thickness dependence; the precessional frequency remains at ~2 GHz for all the permalloy films investigated while α_{eff} drastically decreases with increasing film thickness. These results do not allow a significant correlation of the precessional frequency to the surface morphology to be made. In contrast, the magnetic damping is found to be a very sensitive function of surface roughness, and an unusually high value of α_{eff} of 0.32 was found for the 9 nm thick permalloy film.

Future studies of these systems will be conducted using combinations of pre-patterned substrates, other depostion techniques, and differing modes of excitation. These methods should enable more control over the exact growth of the films so that the surface morphology can be more accurately controlled and the dynamics studied for different geometric constraints. This will allow for a better understanding of the exact mechanisms responsible for the dramatic increase in damping and perhaps lead to accurate control of the damping in future devices.

Chapter 7

References

[1] http://nobelprize.org/nobel_prizes/physics/laureates/2007/press.html

[2] Tim Studt, "Moore's Law continues into the 21st century." R&D Magazine, vol.37 no.12, pp 33-36, (1995)

[3] Amikam Aharoni, "Introduction to the theory of ferromagnetism," Oxford University Press, New York, (2000)

[4] Robert m. White, "Quantum Theory of Magnetism (2nd ed.)," Springer-Verlag, Berlin (1983)

[5] F. Bitter "On inhomogeneities in the Magnetization of Ferromagnetic Materials," Phys. Rev., vol.38, pp 1903-1905, (1931)

[6] Witold Szmaja, "Studies of the surface domain structure of cobalt monocrystals by the SEM type-I magnetic contrast and Bitter colloid method," J. of Mag. and Mag. Mat., vol. 219, pp 281-293 (2000)

[7] Witold Szmaja "Magnetic Microstructure of high-coercivity sintered SmCo5 permanent magnets with conventional Bitter technigue and the colliod-SEM method," Phys. Stat. Sol. vol. 204, no.5, pp 1571-1579 (2007)

[8] C. A. F. Vaz, L. Lopez-Diaz, M. Klaui, et al., "Observation of a geometrically constrained domain wall in epitaxial FCC Co small disks," J. of Mag. and Mag. Mat., vol. 272-276 , pp 1674-1675 (2004)

[9] Robert Fromter, Christian Menk, Holger Stillrich, Hans Peter Oepen, "Imaging the domain pattern of the canted magnetization state of Co/Pt multilayer films," Vacuum, vol 82, pp 395-401 (2008)

[10] M.R. Scheinfein, J. Unguris, M. H. Kelley, D. T. Pierce, and R. J. Celotta, "Scanning electron microscopy with polarization analysis (SEMPA)," Rev.Sci. Instrum., vol 61, pp 2501-2526 (1990)

[11] Chistina Bran, Anna B. Butenko, Nikolai S. Kiselev, et al., "Evollution of stripe and bubble domains in antiferromagnetically coupled [(Co/Pt)8/Co/Ru]18 multilayers," Phys. Rev. B vol. 79 (2009)

[12] Volodymyr A. Chernenko, Ricardo Lopez Anton, Jose M. Barandiaran, et al., "MFM Domain Imaging of Textured Ni-Mn-Ga/MgO(100) Thin Films," IEEE Trans. on Mag. vol. 44 no. 11, pp 3040-3043 (2008)

[13] Jianfeng Yaun, W. Pei, T. Hasagawa, et al., "Study on magnetization reversal of cobalt nanowire arrays by magnetic force microscopy," J. of Mag. and Mag. Mat., vol. 320, pp 736-741 (2008)

[14] U. Schilickum, W. Wulfhekel, and J. Kirschner, "Spin-polarized scanning tunneling microscope for imagning the in-plane magnetization," APL, vol. 83 no.10, pp 2016-2018

[15] M. Bode, A. Kubetzka, K. Von Bergmann, et al., "Imagning the Switching Behavior of Superparamagnetic Nanoislands byy Spin-Polarized Scanning Tunneling Microscopy," Microscopy Research and Technique, vol. 66, pp 117-125 (2005)

[16] M. Bode, "Spin Polarized scanning tunneling microscopy," Rep. Prog. Phys., vol. 66, pp 523-582 (2003)

[17] P. Thakur, J. C. Cezar, N. B. Brookes, R. J. Choudhary, et al., "Direct observation of oxygen induced room temperature ferromagnetism in MoO2 thin films by x-ray magnetic circular dichrosim characterizations," App. Phys. Lett., vol 94, pp 062501-1-3 (2009)

[18] Frederik Wegelin, Alexander Krasyuk, Hans-Joachim Elmers, et al., "Stroboscopic XMCD-PEEM imaging of standing and propagating spinwave modes in permalloy thin-film structures," Surf. Sci., vol. 601, pp. 4694-4699 (2007)

[19] J. Stohr, H. C. Seigmann, "Magnetism; from fundamentals to naonscale dynamics," Springer-Velag, Berlin (2006)

[20] Cesar L. Ordonez-Romero, Boris A. Kalinikos, Pavol Krivosik, et al., "Three-

magnon splitting and confluence processes for spin-wave excitations in yttrium iron garnet-films: Wave vector selective Brillouin light scattering measurements and analysis," Phys. Rev. B. vol. 79, pp 144428-1-8 (2009)

[21] A. A. Stashkevicha, P. Djemia, Y. K. Fetisov, et al., "High-intensity Brillouin light scattering by spin waves in a permalloy film

under microwave resonance pumping," J. Appl. Phys. vol. 102, pp 103905-1-6 (2007)

[22] S. O. Demokritov, B. Hillebrands, A. N. Slavin, "Brillouin light scattering studies of confined spin waves: Linear and nonlinear confinement," Phys. Rep., vol 348, pp 441-489 (2001)

[23] Andreas Neudert, Paul S. Keatley, Volodymyr V. Kruglyak, et al., "Excitation and Imaging of Precessional Modes in Soft-Magnetic Squares," IEEE Trans. on Mag., vol.44, pp 3083-3086 (2008)

[24] B. C. Choi, J. Ho, Y. K. Hong, et al., "Magnetization Switching Dynamics Depending on As-Patterened Magnetization State in Magnetic Thin-Film Elements," IEEE Trans. on Mag., vol. 41 no. 10, pp 2709-2711 (2005)

[25] N.Spiridis, T. Slezak, M. Zajac, and J. Korecki, "Ultrathin epitaxial bcc-Co films stabilized on Au(001)- hex," Surf. Sci., vol. 566-568, pp. 272-277 (2004)

[26] M. R. Freeman, B. C. Choi, "Advances in Magnetic Microscopy," Science, vol. 294, (2001)

[27] Wayne K. Hiebert, "Experimental Micromagnetic Dynamics: Ultrafast Magnetization Reversal Using Time Resolved Scanning Kerr Effect Microscopy," (PhD Thesis) University of Alberta, Edmonton. (2001)

[28] N. L. Schryer and L. R. Walker, "The motion of 180° domain walls in uniform dc magnetic fields," J. Appl. Phys. vol. 45 no. 12, pp 5406-5421 (1974)

[29] David Jiles, "Introduction to Magnetism and Magnetic Materials," Chapman and Hall, NY. NY. (1991)

[30] C. D. Olson, A. v. Pohm, "Flux Reversal in Thin Films of 82% Ni, 18% Fe," J. Appl Phys., vol. 29 no. 3, pp 274-282 (1958)

[31] E. M. Gyorgy, "Rotational Model of Flux Reversal in Square Loop Ferrites," J. Appl. Phys., vol. 28 no. 9, pp 1011-1015 (1957)

[32] M. H. Kryder and F. B. Humphrey, "Dyanmic Kerr Obeservations of High-Speed Flux Reversal and Relaxation processes in Permalloy Thin Films," J. Appl. Phys., vol. 40 no 6, pp 2469-2474 (1969)

[33] G.T. Rado and H. Suhl, eds., "Magnetism III," Academic Press, N.Y. N.Y (1963)

[34] Daniel C. Mattis, "The theory of magnetism made simple : an introduction to physical concepts and to some useful mathematical methods," World Scientific Press, London (2006)

[35] T.L. Gilbert, "A Lagragian formulation of the gyromagnetic equation of the magnetization field," Phys. Rev., vol. 100, pp 1243 (1955)

[36] M. Bauer, R. Lopusnik, J. Fassbender, and B. Hillebrands, "Magnetization reversal in ultrashort magnetic field pulses," J. Mag. and Mag. Mat., vol 218, pp 165-176 (2000)

[37] M. Bauer, J. Fassbender, B. Hillebrands, and R.L. Stamps,"Switching behaviour of a Stoner particle beyond the relaxation time limit," Phys. Rev. B, vol 61 no. 5, pp 3410-3416 (2000)

[38] Q.F. Xiao, J. Rudge, B. C. Choi, et al., "Dynamics of ultrafast magnetization reversal in submicron elliptical Permalloy thin fim elements," Phys. Rev. B, vol. 73, pp 104425-1-5 (2006)

[39] Patrick Bruno, "Dipolar magnetic surface aisotropy in ferromagnetic thin films with interfacial roughness," J. Appl. Phys., vol. 64 no. 6, pp 3153-3156 (1988)

[40] R. Urban, G. Woltersdorf, B. Heinrich, "Gilbert damping in single and multilayer ultrathin films: Role of interfaces in nonlocal spin dynamics," Phys. Rev. Lett. vol 87, 217205-1-4 (2001).

[41] A. Yu. Dobin, R.H. Victora, "Surface roughness induced extrinsic damping in thin magnetic films," Phys. Rev. Lett. 92, 257204-1-4 (2004)

[42] J. B. Youssef, N. Vukadinovic, D. Billet, M. Labrune, "Thickness-dependent magnetic excitations in Permalloy films with nonuniform magnetization," Phys. Rev. B 69, 174402-1-9 (2004)

[43] J. Walowski, et al., "Intrinsic and non-local Gilbert damping in polycrystalline nickel studied by Ti:sapphire laser fs spectroscopy," J. Phys. D: Appl. Phys. 41, 164016-1-10 (2008)]

[44] Th. Gerrits, T.J. Silva, J.P. Nibarger, Th. Rasing, "Large-angle magnetization dynamics investigated by vector-resolved magnetization-induced optical second-harmonic generation," J. Appl. Phys. 96, 6023-6028 (2004)

[45] Grant R. Fowles, "Introduction to Modern Optics, (2nd ed.)" Dover Publications Inc. NY. NY. (1989)

[46] Višňovský, Štefan, "Optics in magnetic multilayers and nanostructures," CRC Taylor & Francis, New York (2006)

[47] Raymond Serway, John W. Jewett, "Physics for Scientists and Engineers volume 1 (6th ed.)," Thomson Learning Inc., Belmont CA (2003)

Chapter 8

Appendices

8.1 Appendix 1: Kerr Effect

The interaction of light and magnetism collectively called magneto-optical effects, come in two broad classes the Farady effect which refers to transmitted light, and the Kerr effect which refers to effects on reflected light. To begin this we first need to introduce Jones matrices. Jones matrices provide a convienient way to deal with polarization changes. For example a left circualrly polarized (LCP) beam can ber represented by (with normalization constants included for completeness) :

$$\frac{1}{2}\begin{bmatrix}1\\ i\end{bmatrix} \tag{8.1}$$

while a right circularly polarized (RCP) beam is given by:

$$\frac{1}{2}\begin{bmatrix}1\\ -i\end{bmatrix} \tag{8.2}$$

Addition of the two vectors gives the result of combining a left and a right circularly polarized beam.

$$1\begin{bmatrix}1\\ 0\end{bmatrix} \tag{8.3}$$

which is a beam linearly polarized along the x axis with an amplitude twice as large as either component.

Jones matrices are readily available for a number of different optical operations. For example a half wave plate has a matrix:

$$\begin{bmatrix} 1 & 0 \\ 0 & -1 \end{bmatrix} \tag{8.4}$$

To find the resultant polarization state of a LCP beam after it transits a half wave plate we use matrix multiplication.

$$\begin{bmatrix} 1 & 0 \\ 0 & -1 \end{bmatrix} * \begin{bmatrix} 1 \\ i \end{bmatrix} = \begin{bmatrix} 1 \\ -i \end{bmatrix} \tag{8.5}$$

So the LCP beam is turned to a RCP beam by the half wave plate. Most texts on optics have some description of Jones matrices. For example Fowles book , "Introduction to Modern Optics," [45] has a short list of optical elements with their associated Jones matirces, as well as a brief description of their use. A quick search of the internet produces a number of related resources.

Now that the Jones matrices have been introduced we can follow the work of Stefan Visnovsky, we begin by noting that the left and right circularly polarized waves have different reflection coefficients.

$$r_{\pm} = \frac{1 - N_{\pm}}{1 + N_{\pm}} \tag{8.6}$$

$$\text{where} \quad : \quad N = n - ik \tag{8.7}$$

where the $\pm$ is used to indicate the two propagation directions, RCP and LCP respectively, and N is the complex index of refraction.

In Cartesian form the the incident and reflected light is given by:

$$\begin{bmatrix} E_x^r \\ E_y^r \end{bmatrix} = \begin{bmatrix} r_{xx} & r_{xy} \\ -r_{xy} & r_{yy} \end{bmatrix} \begin{bmatrix} E_x^i \\ E_y^i \end{bmatrix} \tag{8.8}$$

Here the 2x2 matrix is the cartesian representation of the Jones reflection matrix and the column vectors are the cartesian representation of the electric field.

Transforming this into a CP representation we can write:

$$\begin{bmatrix} E_+^r \\ E_-^r \end{bmatrix} = 2^{-1/2} \begin{bmatrix} r_+ & 0 \\ 0 & r_- \end{bmatrix} \begin{bmatrix} E_x^i - iE_y^i \\ E_x^i + iE_y^i \end{bmatrix} \tag{8.9}$$

We can assume that the initial polarization of the beam is conincident with the x-axis so that the complex terms on the right of equation 8.9 vanish.

$$\begin{bmatrix} E_+^r \\ E_-^r \end{bmatrix} = 2^{-1/2} \begin{bmatrix} r_+ & 0 \\ 0 & r_- \end{bmatrix} \begin{bmatrix} 1 \\ 1 \end{bmatrix} E_x^i = (2^{-1/2})(E_x^i) \begin{bmatrix} r_+ \\ r_- \end{bmatrix} \tag{8.10}$$

Taking the CP representation of the reflected beam and converting it to a Cartesian form again (for ease of comparison)

$$\begin{bmatrix} E_x^r \\ E_y^r \end{bmatrix} = 2^{-1/2} \begin{bmatrix} 1 & 1 \\ i & -i \end{bmatrix} (2^{-1/2})(E_x^i) \begin{bmatrix} r_+ \\ r_- \end{bmatrix} \tag{8.11}$$

$$\begin{bmatrix} E_x^r \\ E_y^r \end{bmatrix} = \frac{1}{2}(E_x^i) \begin{bmatrix} r_+ + r_- \\ i(r_+ - r_-) \end{bmatrix} \tag{8.12}$$

The ratio of the E_y to E_x shows the degree of polarization.

$$\chi_r = \frac{E_y^r}{E_x^r} = \frac{i(r_+ - r_-)}{r_+ + r_-} = i\frac{N_+ - N_-}{N_+N_- - 1} \tag{8.13}$$

From 8.13 it can be seen that if the reflection coeffecients are identical then the degree of polarization given by this ratio is 0 as expected since the initial polarization state was assumed to be entirely along the x-axis. However if the reflection coeffecients differ then we get a non-zero ratio indicating that the electric field after reflection has some (usually small) component in the y direction. This change is the basis of the magneto-optic effect and although the above derivation is only applicable to a beam of normal incidence, similar calculations can be done for other configurations. More details on other configurations can be found in the book "Optics in Magnetic Multilayers and Nanostructures," by Stefan Visnovsky [46]

8.2 Appendix 2: Field Calculation

This appendix shows the mathematica code used to estimate the field strength of the excitation coil. The code is based upon the Biot-Savart law which is given in any elementary text on magnetism, for example Serway's "Physics for Scientists and Engineers." In particular, for an infinitely long thin wire the Biot-Savart law gives the magnetic field at a distance from a current carrying conductor as [47]:

$$B = \frac{\mu_0 I}{2\pi r} \tag{8.14}$$

where: I is the current in the conductor, μ_0 is the permeability of free space ($4\pi * 10^{-7}$), and r is the distance from the conductor to the point of intrest.

We define the following quantities; A field point P(x,y), an infintesimal area within the rectangular coil dA(x_0,y_0), r the vector from dA to P, and α the angle between r and the x axis. With some basic geometry we can rewrite some of these:

$$r = \sqrt{(x - x_0)^2 + (y - y_0)^2} \tag{8.15}$$

$$\sin(\alpha) = \frac{(y - y_0)}{\sqrt{(x - x_0)^2 + (y - y_0)^2}} \tag{8.16}$$

$$\cos(\alpha) = \frac{(x - x_0)}{\sqrt{(x - x_0)^2 + (y - y_0)^2}} \tag{8.17}$$

the current through an infintesimal is the current density:

$$j = \frac{I}{A} \tag{8.18}$$

and finally the component of the field along each direction is given by:

$$dB_x = \frac{\mu_0 j}{2\pi} \frac{\sin(\alpha)}{r} \tag{8.19}$$

$$dBy = \frac{\mu_0 j}{2\pi} \frac{\cos(\alpha)}{r} \tag{8.20}$$

Combining all of this together (ie eqn 8.15 and 8.16 into eqn 8.19) and integrating across the area of the conductor yields:

$$dBx = \frac{\mu_0 I}{2\pi(2xa)(2ya)} \int_{-xa}^{xa} \int_{-ya}^{ya} \frac{(y - y_0)}{[(x - x_0)^2 + (y - y_0)^2]} dy_0 dx_0 \tag{8.21}$$

Evaluating the first integral in equation 8.21 gives:

$$dBx = \frac{\mu_0 I}{2\pi(2xa)(2ya)} \int_{-xa}^{xa} (\frac{-1}{2} Log[(x - x_0)^2 + (y - ya)^2] + \frac{1}{2} Log[(x - x_0)^2 + (y + ya)^2]) dx_0 \tag{8.22}$$

Numerical integration of the integral in 8.22 gives the x component of the magnetic field in Tesla for a given point in space and a similar result can be derrived for the y component. In the folowing code the magnetic field is calculated as a sum of two rectangular conductors. The prefactor of $\frac{1}{2000}$results from the prefactors already shown and $1*10^4$ to convert the units from tesla to gauss.

Code starts here.

(*Calculation of magnetic field near a transmission coil. Each side has a rectangular cross-section of 2xa by 2ya in cm.

xa= half the line width

ya= half the line height

I = the current in Amps

hx = the x component of the field

hy= the y component of the field

*)

Needs ["Graphics'PlotField'"]; um=1/10^6 (*um is now a symbol for 10^-6 m*)

ClearAll[hx1, hy1];

(* setting hx1 and hy1. NIntegrate[fcn, {x0, -xa, xa}] means numeerically integrate fcn WRT x0 between -xa and xa *)

hx1 [x_, xa_, y_, ya_] := NIntegrate[-$\frac{1}{2} Log\ [(x - x0)^2 + (y - ya)^2] + \frac{1}{2} Log[(x - x0)^2 +$

$(y + ya)^2]$, $\{x0, -xa, xa\}$, $AccuracyGoal \rightarrow 6]$;

hy1 [x_, xa_, y_, ya_] := NIntegrate[-$\frac{1}{2} Log\ [(y - y0)^2 + (x - xa)^2] + \frac{1}{2} Log[(y - y0)^2 +$ $(x + xa)^2]$, $\{y0, -ya, ya\}$, $AccuracyGoal \rightarrow 6]$;

hx [I_, x_, xa_, y_, ya_] := $\frac{Ihx1[x,xa,y,ya]}{2000 * xa * ya}$;

hy [I_, x_, xa_, y_, ya_] := $\frac{Ihy1[x,xa,y,ya]}{2000 * xa * ya}$;

coil1=Table[hy[0.9, x um, 10 um, 0.30 um, 0.150 um], {x, 0, 70, 0.1}]; (*only calculating out of plane component here*)

coil2=Table[hy[0.9, x um, 10 um, 0.30 um, 0.150 um], {x, 0, -70, 0.1}];

both=coil2-coil1;

position= Table[x, {x, -35, 35, 0.1}];

field=Transpose[{position,both}];

ListPlot[field];

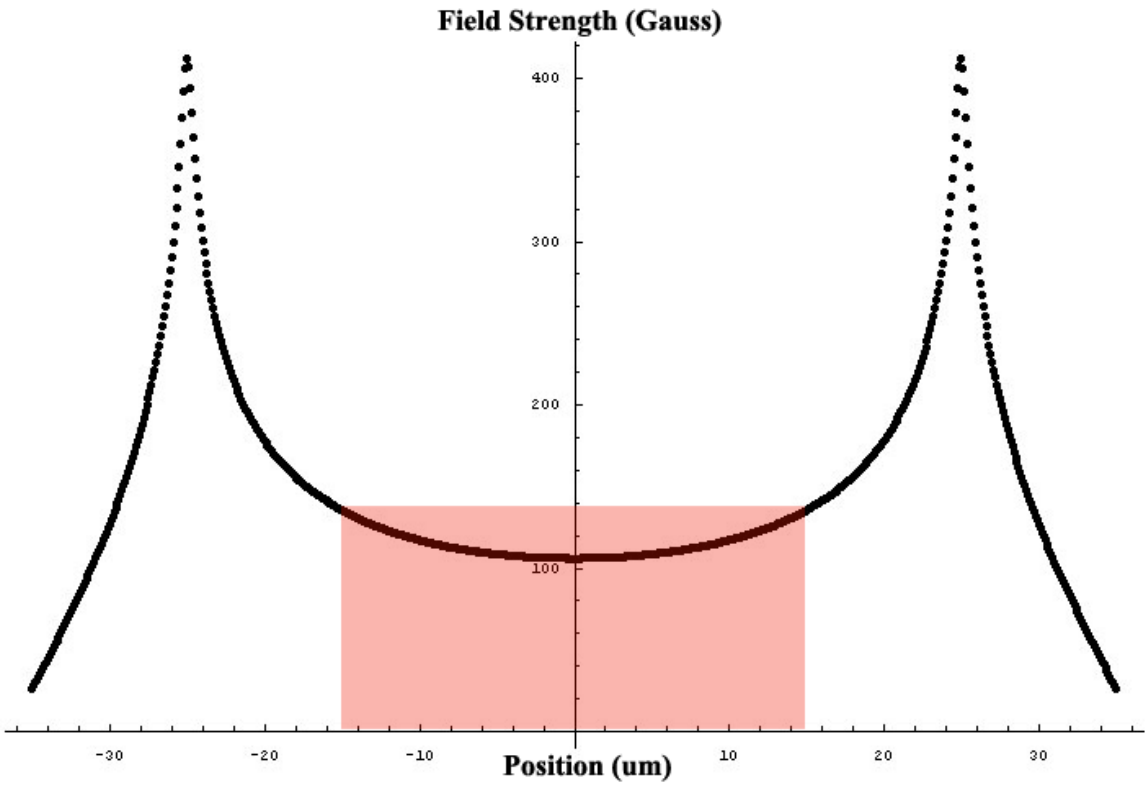

Figure 8-1: Plot of the calculated field distribution. The disconitiuities are from the inside edge of each wire. The rectangle shows the approximate dimensions of the probe beam.